



HAL
open science

Machine-learning and mechanistic modeling of primary and metastatic breast cancer growth after neoadjuvant targeted therapy

Sébastien Benzekry, Michalis Mastri, Chiara Nicolò, John Ebos

► **To cite this version:**

Sébastien Benzekry, Michalis Mastri, Chiara Nicolò, John Ebos. Machine-learning and mechanistic modeling of primary and metastatic breast cancer growth after neoadjuvant targeted therapy. 2023. hal-04384182

HAL Id: hal-04384182

<https://hal.science/hal-04384182>

Preprint submitted on 10 Jan 2024

HAL is a multi-disciplinary open access archive for the deposit and dissemination of scientific research documents, whether they are published or not. The documents may come from teaching and research institutions in France or abroad, or from public or private research centers.

L'archive ouverte pluridisciplinaire **HAL**, est destinée au dépôt et à la diffusion de documents scientifiques de niveau recherche, publiés ou non, émanant des établissements d'enseignement et de recherche français ou étrangers, des laboratoires publics ou privés.

Machine-learning and mechanistic modeling of primary and metastatic breast cancer growth after neoadjuvant targeted therapy

S. Benzekry^{1*}, M. Matri², C. Nicolò³ and J. ML Ebos^{2,4}

1. *Computational Pharmacology and Clinical Oncology (COMPO), Inria Sophia Antipolis–Méditerranée, Cancer Research Center of Marseille, Inserm UMR1068, CNRS UMR7258, Aix Marseille University UM105, 13385 Marseille, France*
2. *Department of Cancer Genetics and Genomics, Roswell Park Comprehensive Cancer Center, Buffalo, NY, USA.*
3. *InSilicoTrials Technologies S.P.A, Riva Grumula 2, 34123, Trieste, Italy.*
4. *Department of Medicine, Roswell Park Comprehensive Cancer Center, Buffalo, NY, USA.*

* Correspondence: Sebastien Benzekry, PhD, sebastien.benzekry@inria.fr

Running title: Mathematical modeling of metastasis after neoadjuvant therapy

Conflict of interest: The authors declare no potential conflicts of interest

Abstract

Clinical trials involving systemic neoadjuvant treatments in breast cancer aim to shrink tumors prior to surgery while simultaneously allowing for controlled evaluation of biomarkers, toxicity, and suppression of distant (occult) metastatic disease. Yet such trials are rarely preceded by preclinical testing involving surgery. Here we used a mouse model of spontaneous metastasis after surgical removal to develop a predictive mathematical model of neoadjuvant treatment response to sunitinib, a receptor tyrosine kinase inhibitor (RTKI). Longitudinal data consisted of measurements of presurgical primary tumor size and postsurgical metastatic burden in 128 mice (104 for model training, 24 for validation), following variable neoadjuvant treatment schedules over a 14-day period. A nonlinear mixed-effects modeling approach was used to quantify inter-animal variability. Machine learning algorithms were applied to investigate the significance of several biomarkers at resection as predictors of individual kinetics. Biomarkers included circulating tumor- and immune-based cells (circulating tumor cells and myeloid-derived suppressor cells) as well as immunohistochemical tumor proteins (CD31 and Ki67). Our simulations showed that neoadjuvant RTKI treatment inhibits primary tumor growth but has little efficacy in preventing (micro)-metastatic disease progression after surgery. Surprisingly, machine-learning algorithms demonstrated only limited predictive power of tested biomarkers on the mathematical parameters. These results suggest that presurgical modeling might be an effective tool to screen biomarkers prior to clinical trial testing. Mathematical modeling combined with artificial intelligence techniques represent a novel platform for integrating preclinical surgical metastasis models in outcome prediction of neoadjuvant treatment.

Major findings: Using simulations from a mechanistic mathematical model compared with preclinical data from surgical metastasis models, we found anti-tumor effects of neoadjuvant RTKI treatment can differ between the primary tumor and metastases in the perioperative setting. Model simulations with variable drug doses and scheduling of neoadjuvant treatment revealed a contrasting impact on initial primary tumor debulking and metastatic outcomes long after treatment has stopped and tumor surgically removed. Using machine-learning algorithms, we identified the limited power of several circulating cellular and molecular biomarkers in predicting metastatic outcome, uncovering a potential fast-track strategy for assessing future clinical biomarkers by paring patient studies with identical studies in mice.

1 Introduction

2 Neoadjuvant trials in breast cancer (BC) patients involve the administration of systemic
3 treatment for a limited period to treat (and reduce) localized primary tumors prior to
4 surgery. They provide several advantages to assist in novel drug development and
5 translational research (1). For example, neoadjuvant trials can be faster to conduct,
6 require fewer patients, offer the potential for controlled assessment of biological tissue
7 for novel biomarker development, and critically, can potentially limit distant (often
8 occult) metastatic lesions to delay disease recurrence long after treatment has ended
9 (1,2). Yet there are surprisingly few studies that precede neoadjuvant trial design to
10 offer predictive guides to validate drug efficacy, biomarkers, or possible outcomes. In
11 this regard, *in silico* (mathematical) modeling and preclinical *in vivo* testing can be
12 useful. However, mathematical modeling most often occurs as post-hoc analysis in BC
13 trials and studies in mice rarely include clinically relevant systems that capture the
14 complexity of surgical impact on primary/metastatic growth to offer rationalized
15 inclusion of biomarkers in trial design.

16 To address this gap, here we describe a mathematical modeling framework of
17 neoadjuvant therapy using a combination of preclinical *in vivo* and *in silico* data to
18 provide a predictive platform for treatment outcomes. This extends from our prior work
19 that validated a semi-mechanistic model comparing localized 'primary' tumor growth
20 with the growth of spontaneous metastatic disease that occurred after surgery in mouse
21 models of BC (4). We used 'ortho-surgical' models (i.e., orthotopic implantation followed
22 by surgical tumor resection) to show that inter-individual variability in the kinetics of
23 metastatic growth could be captured by a (lognormal) distribution of a critical parameter
24 of metastatic aggressiveness, which we termed ' μ '. By adding here neoadjuvant
25 treatment to this mathematical modeling framework it allowed us to; 1) formulate and
26 test mechanistic hypothesis about differential effects on primary versus secondary
27 disease, 2) evaluate the impact of biomarkers on metastatic development and 3)
28 investigate the impact of modulating dosing regimen. In addition, machine learning
29 coupled to mechanistic modeling – an approach that we call 'mechanistic learning' (5,6)
30 – can screen biomarkers with translational potential and establish predictive models
31 (7). In contrast to classical statistical analysis, machine-learning consists in designing
32 models with predictive power as metric of success, rather than inference properties,
33 and makes use of highly nonlinear models such as regression trees or artificial neural
34 networks (8).

35 In this study, we examined neoadjuvant treatment with sunitinib, a molecular targeted
36 tyrosine inhibitor (TKI) that can block angiogenesis-associated vascular endothelial
37 growth factor receptors (VEGFRs) along with several other regulators of metastasis (9).
38 Using a VEGFR TKI had several advantages. First, they have a short half-life which
39 allowed us to confine treatment effects to the presurgical period and incorporate
40 multiple variations of treatment dosing, days treated, and time of resection after initial
41 tumor implantation in mice. Second, VEGFR TKIs have shown mixed effects in the
42 perioperative setting in BC (10). While the addition of neoadjuvant sunitinib to
43 chemotherapy improved pathologic complete response rates, long-term results have
44 been more contrasted, with no disease free survival benefit and either none (11) or
45 some (12) overall benefit. As a monotherapy, we and others have demonstrated that
46 robust inhibition of primary tumor growth does not always translate into inhibition of
47 metastasis post-surgically nor improvement in survival (13–15). In our model, we

48 measured multiple cellular and molecular biomarkers at surgery and used machine
49 learning to investigate their predictive power on the mechanistic parameters of our
50 neoadjuvant mathematical metastatic model. Machine learning confirmed a lack of
51 definitive biomarkers, which shows the value of preclinical modeling studies to identify
52 potential failures that should be avoided clinically.

53

54

55

56

57

58 **Materials and Methods**

59 **Cell lines**

60 The human LM2-4^{LUC+} cells are a luciferase-expressing metastatic variant of the MDA-
61 MB-231 breast cancer cell line derived after multiple rounds of *in vivo* lung metastasis
62 selection in mice, as previously described (16). LM2-4^{LUC+} were maintained in DMEM
63 (Corning cellgro; 10-013-CV) supplemented with 5% v/v FBS (Corning cellgro; 35-010-
64 CV), in a humidified incubator at 37°C and 5% CO₂. The cell line was authenticated by
65 STR profiling (DDC Medical, USA).

66 **Drug and doses used**

67 Sunitinib malate (SU11248; Sutent®®, Pfizer) was suspended in a vehicle formulation
68 that contained carboxymethylcellulose sodium (USP, 0.5% w/v), NaCl (USP, 1.8% w/v),
69 Tween-80 (NF, 0.4% w/v), benzyl alcohol (NF, 0.9% w/v), and reverse osmosis
70 deionized water (added to final volume), which was then adjusted to pH 6. The drug
71 was administered at 60 or 120 mg/kg/day orally by gavage as previously described
72 (13,17). The treatment window used in all neoadjuvant studies consisted of a previously
73 optimized 14-day period prior to surgery (13). Within this 14-day period, daily sunitinib
74 (Su) treatment was given either at 60 mg/kg/day (for 3, 7, or 14 days followed by vehicle
75 for 11, 7, or 0 days, respectively), or at 120 mg/kg/day for 3 days followed by 60
76 mg/kg/day for 0, 4, 8, or 11 days, and vehicle for 11, 7, 3, or 0 days, respectively. An
77 example of an abbreviation in the text includes 'Su60(14D)', which means 'sunitinib at
78 60mg/kg/day for 14 days. Schematics for all studies are shown in Table S1. Mice
79 treated daily with vehicle for 14 days were used as controls. Detailed analysis and
80 comparisons of these treatment regimens are described in a companion study
81 evaluating treatment breaks on metastatic disease.

82 **Ortho-surgical model of metastasis**

83 Animal studies were performed in strict accordance with the recommendations in the
84 Guide for Care and Use of Laboratory Animals of the National Institute of Health and
85 according to guidelines of the Institutional Animal Care and Use Committee at Roswell
86 Park Comprehensive Cancer Center (protocol: 1227M, PI: John M.L. Ebos).

87 *Implantations:* Experimental methodology was extended from previous work using
88 a xenograft animal model of breast cancer spontaneous metastasis that includes
89 orthotopic implantation followed by surgical resection of a primary (termed 'ortho-
90 surgical') (4). Briefly, LM2-4^{LUC+} (1 x 10⁶ cells in 100µl DMEM) were orthotopically
91 implanted into the right inguinal mammary fat pad (right flank) of 6-8-week old
92 female SCID mice, as described previously (4,13,17). Primary tumor burden was
93 monitored with Vernier calipers using the formula width²(length x 0.5) and
94 bioluminescence imaging (BLI) (4,13,17). Neoadjuvant treatments started 14 days
95 before primary tumors were surgically removed at a timepoint (34-38 days post-
96 implantation) previously optimized for maximal distant metastatic seeding but
97 minimal localized invasion (4,13). The surgeries were planned at specific time
98 points post-implantation to avoid invasion of primary tumor into the skin or
99 peritoneal wall, ensuring that metastatic progression had proceed and minimizing
100 the possibility of surgical cure (4,13). Postsurgical MB was assessed by BLI and
101 overall survival was monitored based on signs of end stage disease as previously

102 described(4,13).

103 *Exclusion criteria:* Two scenarios represented instances where animals were
104 excluded from treatment studies. First, if complete removal of primary tumor was
105 not surgically feasible because of local invasion or evidence of advanced metastatic
106 spread(4,17). Second, if no primary or metastatic tumor was ever detected by BLI
107 or visual assessment it was assumed there was lack of tumor-take upon
108 implantation (4,13).

109 *Randomization:* Before treatment initiation animals were randomized by primary
110 tumor size assessed by Vernier calipers to avoid any false results due to unequal
111 tumor burden between groups (18).

112 **Flow cytometry**

113 Peripheral blood was collected in tubes containing lithium heparin (BD Biosciences;
114 365965) by orbital bleeding one day before surgical tumor resection. Non-specific
115 binding was blocked with normal mouse IgG (Invitrogen; 10400C) incubated with whole
116 blood, followed by incubation with an antibody mix. After staining, cells were fixed in a
117 lyse/fix solution (BD Biosciences; 558049), while red blood cells were lysed. Samples
118 were analyzed with a LSR II low cytometer (Becton Dickinson), while data were
119 acquired with FACSDiva software (Becton Dickinson) and analyzed with FCS Express
120 6 (DeNovo software).

121 **Circulating tumor cells (CTC)**

122 The antibody mix for CTC detection of human CTCs in animal models contained a rat
123 anti-mouse CD45 (30-F11) antibody conjugated to PE (Biolegend; 103106) and mouse
124 anti-human HLA conjugated to AlexaFluor 647 (Biolegend; 311416). CD45 staining with
125 a rat anti-mouse CD45 conjugated to FITC (Invitrogen; MCD4501) was used to
126 eliminate any mouse blood cells, whereas human HLA was used to identify CTC
127 (human LM2-4^{LUC+}). For a positive control, LM2-4^{LUC+} cells were trypsinized, washed
128 with PBS, and stained for both CD45 and HLA. LM2-4^{LUC+} were used to define the CTC
129 gate.

130 **Circulating myeloid-derived suppressor cells (MDSC)**

131 The antibody mix for detection of MDSCs contained a rat anti-mouse CD45 (30-F11)
132 antibody conjugated to PE (Biolegend; 103106), a rat anti-mouse Ly-6G/Ly-6C (Gr1)
133 (RB6-8C5) antibody conjugated to PE-Cy7 (BD Pharmingen; 552985), and a rat anti-
134 mouse CD11b (M1/70) antibody conjugated to eFluor450 (eBioscience; 48-0112).
135 Mouse CD45 staining was used to select only leukocytes, and CD11b and Gr1 were
136 used to define the granulocytic and monocytic MDSC.

137 **Immunofluorescence**

138 Resected tumors were frozen on dry ice in cryo-embedding compound (Ted Pella, Inc;
139 27300), sectioned, and fixed in a 3:1 mixture of acetone:ethanol. Non-specific binding
140 was blocked with 2% BSA in PBS, followed by staining with antibody mix containing
141 rabbit anti-mouse Ki67 antibody (Cell Signaling Technologies; 12202) and rat anti-
142 mouse CD31 antibody (Dianova; DIA-310). Detection of primary antibodies was
143 achieved using FITC conjugated goat anti-rabbit IgG (BD Pharmingen; 554020) and
144 Cy3 conjugated goat anti-rat IgG (Invitrogen; A10522). Samples were counterstained
145 with DAPI (Vector; H-1500) and mounted with a hard-set mounting medium for
146 fluorescence. Random images from each section were obtained with a Zeiss

147 Axiolmager A2 epifluorescence microscope at 200x magnification, and analyzed with
 148 ImageJ. CD31+ cells (% area) and Ki67+ cells (% cells) were quantified automatically
 149 using macro functions, whereas Ki76+/CD31+ cells (proliferating endothelial cells) were
 150 quantified manually.

151 **Mechanistic model of ortho-surgical metastasis**

152 For untreated animals, we previously validated a mechanistic model for description of
 153 pre-surgical primary tumor and post-surgical metastasis kinetics in the ortho-surgical
 154 LM2-4^{LU^C+} animal model (4). Briefly, metastatic development is decomposed into two
 155 main processes: growth and dissemination.

156 Growth of the primary and metastases follow the Gomp-Exp model (19):

$$157 \quad g_p(v) = g(v) = \min\left(\lambda v, \left(\alpha - \beta \ln\left(\frac{v}{V_0}\right)\right)\right),$$

158 where g_p and g denote the growth rates of the primary and secondary tumors,
 159 respectively. Parameter λ limits the Gompertz growth rate to avoid unrealistically fast
 160 kinetics for small sizes and is given by the *in vitro* proliferation rate, assessed previously
 161 (4). Parameters α and β are the Gompertz parameters, and V_0 is the size of one cell (in
 162 units of mm³ for the PT, and photons/seconds for the metastases). The PT volume,
 163 $V_p(t)$ thus solves

$$164 \quad \begin{cases} \frac{dV_p}{dt} = g_p(V_p) \\ V_p(t=0) = V_i, \end{cases}$$

165 with V_i the volume corresponding to the number of cells injected (= 1 mm³ based on the
 166 conversion rule 1 mm³ \approx 10⁶ cells (20)).

167 Dissemination occurs at the following volume-dependent rate (4):

$$168 \quad d(V_p) = \mu V_p,$$

169 where parameter μ can be interpreted as the daily probability that a cell from the PT
 170 successfully establishes a metastasis (4).

171 The metastatic process was described through a function $\rho(t, v)$ representing the
 172 distribution of metastatic tumors with size v at time t . It solves the following initial
 173 boundary value problem (21):

$$174 \quad \begin{cases} \partial_t \rho(t, v) + \partial_v (g(v) \rho(t, v)) = 0, & t \in (0, +\infty), v \in (V_0, +\infty) \\ g(t, V_0) \rho(t, V_0) = d(V_p(t)), & t \in (0, +\infty) \\ \rho(0, v) = 0, & v \in (V_0, +\infty) \end{cases}$$

175 The first equation derives from a balance equation on the number of metastases; the
 176 second equation is a boundary condition for the rate of newly created metastases; the
 177 third equation is the initial condition (no metastases exist at the initial time).

178 The total MB at time t was then given by

$$179 \quad M(t) = \int_{V_0}^{+\infty} v \rho(t, v) dv = \int_0^t d(V_p(t-s)) V(s) ds,$$

180 which can be solved efficiently through the use of a fast Fourier transform algorithm
 181 (22). In the previous equation, $V(s)$ represents the volume reached by a metastatic
 182 tumor after a period of time s from its emission, when growing with growth rate g .

183 **Mechanistic model of neoadjuvant targeted therapy**

184 Using this model, we next incorporated the effects of systemic therapy. This new model
 185 includes neoadjuvant sunitinib treatment and assumes that the drug reduces the
 186 primary tumor growth rate by a term proportional to its concentration, $C(t)$ (Norton-
 187 Simon hypothesis (23)):

$$188 \quad g_p^T(t, v) = g_p(v)(1 - k C(t))$$

189 where k is a parameter of drug efficacy. As no pharmacokinetic data was available, we
 190 used a kinetics-pharmacodynamics (K-PD) approach. Namely, we considered that the
 191 drug concentration decays exponentially after each dose,

$$192 \quad C(t) = \frac{1}{V_d} \sum_{i=1}^n D_i e^{-k_e(t - \tau_i)} \mathbb{I}_{t > \tau_i},$$

193 where D_i indicates the dose administered at time τ_i . The volume of distribution V_d and
 194 the elimination rate constant k_e were fixed to the values reported in (24). Inclusion of
 195 treatment effect on metastatic growth was considered in the model development phase;
 196 however, this led to model predictions which could not explain the behavior of the
 197 experimental data. Therefore, the final model considered that sunitinib did not affect
 198 growth of metastases during neoadjuvant treatment.

199 **Calibration of the mathematical metastatic model and parameter** 200 **estimation**

201 Following previously established methodology (4), the mathematical metastatic model
 202 was fitted to the experimental data using a nonlinear-mixed effects modeling approach
 203 (25). Briefly, this consists in modeling inter-animal variability by assuming a parametric
 204 distribution for the model parameters. All individual PT and MB longitudinal data could
 205 then be pooled together in a population model, whose parameters were estimated by
 206 likelihood maximization (25). In mathematical terms, if y_j^i denotes the observation
 207 (primary tumor size or metastatic burden) in animal i at time t_j^i and $f(t_j^i; \theta^i)$ denotes
 208 the model value in an animal with parameter set $\theta^i = (\alpha^i, \beta^i, k^i, \mu^i)$, the statistical model
 209 linking the model to the observations writes:

$$210 \quad y_j^i = f(t_j^i; \theta^i) + \sigma_j^i \varepsilon_j^i,$$

$$211 \quad \ln(\theta^i) = \ln(\theta_{pop}) + \eta^i, \quad \eta^i \sim \mathcal{N}(0, \Omega)$$

212 where $\varepsilon_j^i \sim \mathcal{N}(0, 1)$ is a gaussian noise for measurement error. The parameters θ_{pop} and
 213 Ω characterize the entire population. The observed data were log-transformed and a
 214 proportional error model was used, that is

$$215 \quad \ln y_j^i = \ln(f(t_j^i; \theta^i)) (1 + \bar{\sigma} \varepsilon_j^i).$$

216 For the vector of individual parameters, a log-normal distribution with full covariance
 217 matrix was assumed. Maximum likelihood estimates of the population parameters were
 218 obtained using the Stochastic Approximation of Expectation-Maximization (SAEM)
 219 algorithm implemented in the nlmeftsa Matlab function (26). PT and MB data were fitted

220 simultaneously for vehicle and sunitinib-treated animals. Visual predictive checks
221 (VPC), individual fits and standard diagnostic graphical tools based on individual
222 parameters were used for evaluating the adequacy of the different model components.

223 **Machine learning algorithms**

224 Effects of covariates on the model parameters were assessed using linear regression
225 and a number of machine learning regression techniques (partial least squares, artificial
226 neural networks, support vector machines and random forest models) using the R caret
227 package (27,28). Except for the random forest models, data were centered and scaled
228 prior to modeling. Tuning parameter values of the regression models were selected to
229 minimize the root mean squared error (RMSE) using five replicates of a 10-fold cross-
230 validation. If θ^i are the true values and $\hat{\theta}^i$ the predicted ones, the RMSE is defined by:

231
$$RMSE = \sqrt{\frac{\sum_i |\hat{\theta}^i - \theta^i|^2}{N}}.$$

232

233

Results

234

***In vivo/in silico* modeling of neoadjuvant treatment**

235

236

237

238

239

240

241

242

243

244

245

246

We have previously developed mathematical parameters of untreated spontaneous systemic metastatic breast cancer using orthotopic tumor implantation and surgical resection (i.e., 'ortho-surgical') models (4). Using individual longitudinal presurgical primary tumor (PT) and postsurgical metastatic burden (MB; tracked by bioluminescence) data, we previously established that the metastatic potential parameter μ quantifies inter-individual variability after surgical resection of the PT (4). In addition, our results validated the use of the mathematical model to simulate pre- and post-surgical metastatic development. Here, using a xenograft model with highly-metastatic human breast cells expressing luciferase (LM2-4^{LUC+}), we evaluated PT and MB data from 128 mice that received multiple doses and durations of neoadjuvant sunitinib treatment over a 14 days period (schematic shown in Fig 1A; see Table S1 and methods for treatment details).

247

248

249

Simulations of neoadjuvant sunitinib targeted treatment therapy (NATT) suggests limited effect on metastasis growth

250

251

252

253

254

255

256

257

258

259

260

261

262

263

264

265

266

267

268

269

We have previously utilized ortho-surgical metastasis models to evaluate the impact of multiple VEGFR TKIs on PT and MB progression (13,14). These studies uncovered that neoadjuvant targeted therapy (NATT) yielded differential effects with suppression of presurgical PT growth not consistently translating into reduction in postsurgical MB nor improvement in survival (13). This effect could result from two phenomena that are mixed in MB quantification: 1) metastatic growth suppression and 2) reduction of metastatic spread as a consequence of primary tumor size reduction. To disentangle the two and qualitatively assess the effect of NATT, we generated predictive model scenarios under two assumptions. In 'scenario A', NATT would have growth-arresting effects on both PT and MB, while in 'scenario B' NATT would have effect only on PT (schematic shown in Fig 1B). To test this, we used our previously calibrated ortho-surgical model of pre- and postsurgical growth using LM2-4^{LUC+} tumor cells grown in SCID mice (4), and only set either both growth rates g_p and g (Scenario 'A') or g_p only (Scenario 'B') to zero during NATT. Scenario 'A' clearly failed to describe the data (Figs 1C and S1), whereas Scenario 'B' interestingly demonstrated good accuracy given that simulations were pure predictions that did not make use of the data for parameter estimation (Figs 1C and S1). These results demonstrate a differential effect of NATT on growth of primary and secondary tumors and suggest that a mathematical model of NATT in our breast cancer ortho-surgical animal model should not include anti-growth effect on metastasis.

270

271

272

Calibration and validation of a kinetics-pharmacodynamics (K-PD) model for pre- and post-surgical disease after neoadjuvant sunitinib therapy

273

274

275

276

To further link dose and scheduling to response, we developed a K-PD metastatic model of NATT using a defined neoadjuvant treatment window (14 days) containing multiple treatment periods (3, 7, 11, 14 days), doses (60mg and 120mg), and time of surgery after tumor implantation (Day 34 or 38) (see Table S1 and methods for details).

277 Following our findings above, we only adapted the PT growth rate g_p from (4), using
278 the Norton-Simon hypothesis for PT anti-growth effect of NATT (23). Estimates of the
279 model parameters are reported in Table 1 and demonstrate high practical identifiability
280 (relative standard error $\leq 17\%$), likely owing to the large number of subjects in the
281 population fit. Confirming our previous results (4), the metastatic potential parameter μ
282 was found to vary significantly amongst individuals (largest coefficient of variation).
283 Visual predictive checks for both vehicle group and treated groups demonstrated
284 accurate goodness-of-fit both at the population (Figs 2A and S2) and individual (Figs
285 2B and S3) levels. In addition, model predictions in independent data sets not used for
286 parameter calibration, with distinct time of surgery (day 38 versus day 34) and drug
287 regimens, were in good agreement with the data (Fig S4). Further model diagnostic
288 plots demonstrated no clear misspecification of the structural and residual error model
289 (Fig S5). Distributions of the empirical Bayes estimates were in agreement with the
290 theoretical distributions defined in the statistical model (Fig S6). Moreover, the η -
291 shrinkage was less than 20% for each parameter, meaning that the individual
292 parameter estimates and the diagnostic tools based on them can be considered reliable
293 (29). Finally, correlations found between the estimated random effects (Fig S7)
294 confirmed the appropriateness of a full covariance matrix in the assumed distribution of
295 the individual parameters. Together, these results show the validity of our mathematical
296 model to simulate PT and MB kinetics under a wide range of NATT administration
297 regimens, which can thus be employed to explore *in silico* the quantitative impact of
298 possible NATT schedules.

299

300 **Simulations of NATT duration reveal contrasted impact on PT size** 301 **reduction and metastasis-free survival**

302 The overall impact of NATT is the combination of i) PT debulking (which in turn reduces
303 metastatic spread from the PT), and ii) an increased risk of metastatic relapse due to
304 delayed removal of the PT. To quantify the impact of NATT duration on these two
305 opposite aspects, we ran simulations of our calibrated model for 0 to 18 days NATT
306 and three dose levels (60, 120 and 240 mg/kg, see Fig 3). First using only the typical
307 population estimates of the parameters (median individual), we found an important
308 increase in postsurgical MB for long NATT: final values ranged from 2.73×10^8 to 7.52
309 $\times 10^8$ cells for NATT durations from 0 to 18 days (176% increase), respectively, at the
310 60 mg/kg dose level (Fig 3A). This is consistent with our model where NATT does not
311 affect metastatic growth, thus delaying surgery can only increase MB. This was less
312 important in higher dose levels (125% and 48.5% increases for 120 mg/kg and 240
313 mg/kg, respectively). To study the impact of inter-individual variability, we leveraged
314 our mixed-effects framework to perform population simulations and quantify final
315 outcome. Namely, we simulated 1000 virtual individuals and recorded the percent
316 changes in PT size at the end of NATT. Fig 3B shows the resulting median PT percent
317 changes, together with an area covering 80% of the population. In addition, we
318 calculated a risk of metastatic relapse from the resulting simulation of MB kinetics. To
319 do so, we considered as MB relapse threshold the 30th percentile of the control
320 population MB at 85 days (considered to be an approximation of long term), to mimic
321 the human situation in which 30% of breast cancer patients with localized disease
322 undergo metastatic relapse (30). This threshold then allowed us to compute the percent
323 of subjects having metastatic relapse in the virtual populations, under varying NATT
324 duration (Fig 3B, circled line). For 60 mg/kg and 120 mg/kg doses, metastatic relapse

325 risk is predicted to increase drastically when delaying PT removal too long. However,
326 for a 240 mg/kg dose (or for virtual subjects with increased sensitivity to treatment),
327 increase in metastatic relapse risk is more moderate, since a prolonged NATT is
328 associated with large decrease of the PT size, thus reducing the source of metastasis.
329 Together, these results illustrate how our mathematical model, informed from preclinical
330 data of an NATT ortho-surgical model, can provide informative quantitative simulations
331 of the impact of treatment schedules. Our findings suggest a moderate to detrimental
332 impact of long sunitinib NATT at low dose, in breast cancer.

333

334 **Machine learning for prediction of the metastatic aggressiveness** 335 **parameter μ from biomarkers at surgery**

336 Next, we wanted to determine whether biological parameters at the time of PT surgery
337 but after NAT had stopped could be utilized as predictive biomarkers of postsurgical
338 MB after treatment cessation. These biomarkers included immunohistochemical
339 molecular protein measurements of resected PT for cell proliferation (Ki67) and blood
340 vessel (CD31) markers in resected PTs (Fig 4A; example shown), blood-based cellular
341 measurements of circulating myeloid derived stromal cells (MDSCs) (Fig 3B), and
342 circulating tumor cells (CTCs) from 66 animals (Fig 4B and 4C, respectively; examples
343 of flowcytometric gating shown). We investigated whether these molecular and cellular
344 biomarkers may parallel the observed variability in the mathematical parameters, in
345 particular μ , whose large variability indicated potential animal subpopulations of
346 variable metastatic potential values. We first examined correlations between
347 biomarkers in order to identify potential redundancies in the data (Fig 4B). High
348 correlations were found between Ki67 and Ki67+/CD31- ($r = 0.979$, $p < 10^{-12}$) and CTC
349 and gMDSC ($r = 0.678$, $p = 3.95 \cdot 10^{-10}$). Next, we investigated the value of these
350 measurements as predictive biomarkers of the mechanistic parameters: α and β
351 capture growth kinetics, k the effect of treatment and μ metastatic dissemination. Fig
352 4B shows correlations between biomarkers and the parameter estimates. As the
353 individual growth parameters α and β were highly correlated ($r = 0.997$, $p < 10^{-5}$), we
354 used the Gompertz tumor doubling time at the volume $V_i = 1 \text{ mm}^3$ to assess the impact
355 of covariates on the tumor growth parameters. It is defined by $DT = -\frac{1}{\beta} \ln \left(\frac{\ln(2)+A}{A} \right)$,

356 with $A = \ln \left(\frac{V_i}{V_0} \right) - \frac{\alpha}{\beta}$. A weak correlation was found between $\log(DT)$ and mMDSC
357 levels (Fig 4E, $r = 0.275$, $p = 0.0257$). However, none of the available biomarkers was
358 found to correlate either with μ or $\log(\mu)$ (Fig S8). Next, partial least squares and a
359 number of different machine learning regression algorithms were tested in order to
360 identify possible relationships between covariates and individual estimates of the
361 metastatic potential parameter (shown in Fig 1A schematic). These included neural
362 networks, support vector machines and random forest models (31). Cross-validation
363 results for the RMSE of the final regression models were compared against the
364 intercept-only model (the constant model where predictions are the same for all animals,
365 given by the median value in the population, μ_{pop}). As shown in Figs 4F and 4G, none
366 of the fitted models had RMSE or R^2 significantly different from the intercept-only model.
367 Lowest RMSE was achieved by the intercept-only model. Values of R^2 ranged from
368 0.133 to 0.199 across the models, with the highest value reached by the conditional
369 random forest model. Prediction error on $\ln(\mu)$ ranged from $9.83\% \pm 10.7\%$ for the best
370 model (conditional random forests, mean \pm std) to $10.6\% \pm 11.3\%$ for the worse

371 (random forests), which was not superior to predictive power of the intercept-only model
372 ($9.71\% \pm 10.1\%$). Plotting the observed versus predicted values (Figs 5 and S9)
373 confirmed that the fitted algorithms were unable to explain the variability of parameter
374 μ . Together, these results demonstrate that the biomarkers considered in this study
375 have limited predictive power for metastatic potential as defined by μ .

376

Discussion

378 A large part of *in vivo* studies in experimental therapeutics focus on the effect of
379 treatments on isolated tumors and few make use of metastatic animal models (32).
380 However, we and others have previously shown that differential effects occur on the
381 primary tumor and the metastases for some anti-cancer drugs, such as the
382 multitargeted tyrosine kinase inhibitor sunitinib (13,14,33). Similarly, apart from efforts
383 focusing on evolutionary dynamics of metastasis that do not make use of longitudinal
384 data on size kinetics (34), few quantitative mathematical models exist for metastatic
385 development (4,21,35,36), and none has been quantitatively validated for systemic
386 therapy beyond theoretical considerations (35,37,38). In previous work we first
387 established such a mathematical model featuring natural metastatic development and
388 surgery of the primary tumor, but no systemic treatment (4). This was a critical step
389 before being able to model the effect of systemic treatments such as NATT where
390 treatments are limited and long-term benefits are presumed but difficult to quantify as
391 disease recurrence can happen years after surgery, or not recur at all. In the current
392 study, we extended our mathematical model to examine NATT with the RTKI sunitinib
393 by using longitudinal data of 128 mice (more than four times more than previous studies
394 (4,36)). Such large number of subjects and tightly controlled experimental conditions
395 (genetically identical animal background, cell origin, treatment periods, etc..), resulted
396 in precise estimates of the model parameters. Together our results represent an
397 idealized system for predicting treatment impact and novel biomarker identification that
398 could assist in trial design prior to testing in patients.

399 Our results using sunitinib showing efficacy in reducing primary tumor growth but not
400 metastasis mirror our previous report with two ortho-surgical animal models where we
401 found that NATT with sunitinib and axitinib (another VEGFR TKI) did not always limit
402 metastatic disease after surgery, despite clear antitumor effects on localized disease
403 (13). This represents a challenge observed clinically with RTKIs where, despite
404 decades of potent tumor reducing effects in mouse models, efficacy in patients with
405 metastatic disease could be underwhelming. Using our mathematical model to simulate
406 distinct biological scenarios, we demonstrated that the effect of the drug on tumor
407 growth could differ between primary and secondary sites. Conversely, model simulation
408 predictions (with no fitting involved) of a scenario where metastatic development during
409 NATT was only altered by primary tumor size shrinkage was in excellent agreement
410 with the data.

411 These findings could be explained by the fact that the primary tumor (in the mammary
412 fat pad) and the secondary tumors (mostly in the lungs) would rely on different growth
413 mechanisms, especially at small sizes. Supporting this explanation, a study showed
414 that metastasis relied more on vessel co-option rather than angiogenesis, thus
415 providing them a mechanism of resistance to VEGFR TKIs therapy (39). Beyond NATT,
416 our model predicts limited efficacy of sunitinib in the postsurgical setting, because
417 metastases would likely be similarly small and rely on similar growth mechanisms.
418 Interestingly, recent experimental results in mice confirmed this prediction where, using
419 a similar metastatic experimental system of triple negative breast cancer, adjuvant
420 sunitinib did not improve survival (40). The mechanistic model of NATT validated here
421 provides a valuable tool to explore the impact of the treatment schedules on response

422 and relapse. Simulating varying durations and doses of NATT, we found that long
423 durations of NATT could significantly increase the risk of metastatic relapse when PT
424 response was moderate. Further, our model provides the computational basis to
425 analyze the impact of various NATT dosing regimen in terms of sequence, breaks and
426 frequency, which is the topic of a companion work.

427 For breast cancer patients diagnosed with localized disease, predicting the risk and
428 timing of distant metastatic relapse is a major clinical concern (41–43). Accurate ways
429 to predict the extent of invisible metastatic disease at diagnosis and risk of future
430 metastatic relapse could help to personalize perioperative therapy protocols, and avoid
431 highly toxic therapies to patients with low risk of relapse (42). However, only two risk
432 models (44,45) have met the AJCC criteria for prognostic tool quality so far (46), and
433 both rely on classical Cox regression survival models. Recently, we have developed a
434 mechanistic approach to metastatic relapse prediction (47). However, this work did not
435 include the impact of NATT not any systemic treatment. The mathematical model that
436 we validated here on animal data combined with the methodology developed in (47)
437 lays the groundwork for applications in the clinical NATT setting. It could further refine
438 individual predictions of metastatic relapse in breast cancer by providing surrogate
439 markers of long-term outcome additional to pathologic complete response (3). Indeed,
440 the NATT time period represents an invaluable window of opportunity to gather both
441 longitudinal data (such as kinetics of tumor size or pharmacodynamic marker, or
442 circulating DNA from liquid biopsies) and one-time biomarkers from tumor tissue (2).
443 Here, we propose that mathematical models could form the basis of digital tools able
444 to integrate this multi-parametric and dynamic data into predictive algorithms of both
445 long-term outcome and disease sensitivity to systemic therapy in case of distant
446 relapse.

447 In the era of artificial intelligence (48), it is to be expected that an increasing number of
448 such prognosis models will appear, combining advances in cancer biology (e.g.
449 molecular gene signatures (42,49)) and imaging (50,51) with algorithmic engineering.
450 Recent years have witnessed the generalization of methods going beyond classical
451 statistical analysis, grouped by the generic term of machine learning (ML) (52).
452 However, these techniques have not been applied to preclinical data from targeted
453 therapy. Here, we proposed an approach to combine ML with mechanistic modeling
454 that consists of using biomarkers at surgery to predict individual mathematical
455 parameters and subsequently postsurgical metastatic evolution. Multiple cellular and
456 molecular biomarkers were measured at the time of surgery, either by
457 immunohistochemistry or flow cytometry. These constituted candidate features for ML
458 prediction of the critical parameter μ , which we found as being the major driver of inter-
459 subject metastatic variability. We found overall that these biomarkers contained only
460 limited predictive power of μ , suggesting that alternative biomarkers should be explored
461 in future preclinical and clinical studies. This contrasts with reports showing Ki67 as
462 significantly associated with risk of metastatic relapse (53). It might be due to the fact
463 that Ki67 is a proliferation marker (54), which should rather be predictive of α or the
464 doubling time. In fact, such correlation was observed between Ki67+/CD31+ and DT
465 (Fig 3E), as well as clinical work using our modeling approach (47). Paired with early
466 clinical trials, our *in vivo/in silico* approach could have translational value to inform the
467 screening of biomarkers.

468 Important limitations of our study are that we only analyzed data from one tumor type
469 (triple negative breast cancer), one cell line in one, immune-depressed, animal system

470 and one drug. On the other hand, this is a necessary prerequisite to control as much
471 as possible the heterogeneity in the data, which still remains substantial despite a tightly
472 controlled experimental setting. Such conditions ensure robust test of biological
473 assumptions underlying our mathematical models and, eventually, refutation of
474 unplausible ones (here, that primary and secondary growth would be equally
475 suppressed by NATT). Nevertheless, to address these limitations, we conducted a
476 companion study in similar ortho-surgical kidney cancer systems, with two cell lines
477 (SN12-PM6-N and RENCA, respectively of human and murine origin), immune-
478 competent animals (Balb/c mice for the RENCA cells), and two VEGFR TKIs (Sunitinb
479 and Axitinib) used in the clinical setting to treat kidney cancer patients. In addition, we
480 investigated in depth the impact of breaks and high-dose “bursts” during NATT. The
481 mathematical model developed on the basis of the one in this study allowed to i)
482 demonstrate and quantify post-NATT PT growth rebound and ii) quantify the impact of
483 such dosing regimen variations on post-surgical metastatic development.

484 Given the increasingly diverse arsenal of systemic anti-cancer therapies available with
485 the approval of immune-checkpoint inhibitors, optimal treatment sequence (5,55–57)
486 and dosing regimen (58,59) are becoming crucial issues. Our model could be used and
487 extended to guide the rational design of treatment schedules and modes of combination
488 of immunotherapy with another systemic drug, before preclinical or clinical testing. For
489 immunotherapy, the model would need to be developed further and at least include an
490 additional systemic variable representing the immune system. Immuno-monitoring
491 quantifications could provide an invaluable source of longitudinal data to feed
492 mechanistic models (60). In addition, response to neoadjuvant therapy could be used
493 to predict which patients are more likely to benefit from adjuvant therapy (12).
494 Combining artificial intelligence techniques with mechanistic modeling, our modeling
495 methodology offers a way to perform such predictions quantitatively and possibly
496 personalize therapeutic intervention.

497

References

1. Escrivá-de-Romaní S, Arumí M, Zamora E, Bellet M. Neoadjuvant Model as a Platform for Research in Breast Cancer and Novel Targets under Development in this Field. *Breast Care*. Karger Publishers; 2018;13:251–62.
2. Marron TU, Galsky MD, Taouli B, Fiel MI, Ward S, Kim E, et al. Neoadjuvant clinical trials provide a window of opportunity for cancer drug discovery. *Nat Med*. Nature Publishing Group; 2022;28:626–9.
3. Conforti F, Pala L, Bagnardi V, De Pas T, Colleoni M, Buyse M, et al. Surrogacy of Pathologic Complete Response in Trials of Neoadjuvant Therapy for Early Breast Cancer: Critical Analysis of Strengths, Weaknesses, and Misinterpretations. *JAMA Oncol*. 2022;8:1668–75.
4. Benzekry S, Tracz A, Mastri M, Corbelli R, Barbolosi D, Ebos JM. Modeling spontaneous metastasis following surgery: an in vivo-in silico approach. *Cancer Res*. 2016;76:535–47.
5. Ciccolini J, Barbolosi D, André N, Barlesi F, Benzekry S. Mechanistic Learning for Combinatorial Strategies With Immuno-oncology Drugs: Can Model-Informed Designs Help Investigators? *JCO Precis Oncol*. American Society of Clinical Oncology; 2020;486–91.
6. Benzekry S. Artificial intelligence and mechanistic modeling for clinical decision making in oncology. *Clin Pharmacol Ther*. 2020;108:471–86.
7. Rajkumar A, Dean J, Kohane I. Machine Learning in Medicine. *N Engl J Med*. 2019;380:1347–58.
8. Breiman L. Statistical modeling: the two cultures. *Stat Sci Rev J Inst Math Stat*. 2001;16:199–231.
9. Faivre S, Demetri G, Sargent W, Raymond E. Molecular basis for sunitinib efficacy and future clinical development. *Nat Rev Drug Discov*. Nature Publishing Group; 2007;6:734–45.
10. Aalders KC, Tryfonidis K, Senkus E, Cardoso F. Anti-angiogenic treatment in breast cancer: Facts, successes, failures and future perspectives. *Cancer Treat Rev*. 2017;53:98–110.
11. von Minckwitz G, Eidtmann H, Rezai M, Fasching PA, Tesch H, Eggemann H, et al. Neoadjuvant chemotherapy and bevacizumab for HER2-negative breast cancer. *N Engl J Med*. 2012;366:299–309.
12. Bear HD, Tang G, Rastogi P, Geyer CE, Robidoux A, Atkins JN, et al. Bevacizumab added to neoadjuvant chemotherapy for breast cancer. *N Engl J Med*. 2012;366:310–20.
13. Ebos JML, Mastri M, Lee CR, Tracz A, Hudson JM, Attwood K, et al. Neoadjuvant antiangiogenic therapy reveals contrasts in primary and metastatic tumor efficacy. *EMBO Mol Med*. 2014;6:1561–76.

14. Ebos JML, Lee CR, Cruz-Munoz W, Bjarnason GA, Christensen JG, Kerbel RS. Accelerated metastasis after short-term treatment with a potent inhibitor of tumor angiogenesis. *Cancer Cell*. 2009;15:232–9.
15. Ebos JML. Prodding the Beast: Assessing the Impact of Treatment-Induced Metastasis. *Cancer Res*. 2015;75:3427–35.
16. Ebos JML, Lee CR, Bogdanovic E, Alami J, Van Slyke P, Francia G, et al. Vascular endothelial growth factor-mediated decrease in plasma soluble vascular endothelial growth factor receptor-2 levels as a surrogate biomarker for tumor growth. *Cancer Res*. 2008;68:521–9.
17. Matri M, Tracz A, Lee CR, Dolan M, Attwood K, Christensen JG, et al. A Transient Pseudosenescent Secretome Promotes Tumor Growth after Antiangiogenic Therapy Withdrawal. *Cell Rep*. 2018;25:3706-3720.e8.
18. Suresh K. An overview of randomization techniques: An unbiased assessment of outcome in clinical research. *J Hum Reprod Sci*. 2011;4:8–11.
19. Wheldon TE. *Mathematical Models in Cancer Research*,. 1 edition. Bristol: CRC Press; 1988.
20. Spratt JS, Meyer JS, Spratt JA. Rates of growth of human solid neoplasms: Part I. *J Surg Oncol*. 1995;60:137–46.
21. Iwata K, Kawasaki K, Shigesada N. A dynamical model for the growth and size distribution of multiple metastatic tumors. *J Theor Biol*. 2000;203:177–86.
22. Hartung N. Efficient resolution of metastatic tumor growth models by reformulation into integral equations. *Discrete Contin Dyn Syst Ser B*. 2015;20:445–67.
23. Norton L, Simon R. Tumor size, sensitivity to therapy, and design of treatment schedules. *Cancer Treat Rep*. 1977;61:1307–17.
24. Zhou Q, Gallo JM. Quantification of sunitinib in mouse plasma, brain tumor and normal brain using liquid chromatography-electrospray ionization-tandem mass spectrometry and pharmacokinetic application. *J Pharm Biomed Anal*. 2010;51:958.
25. Lavielle M. *Mixed Effects Models for the Population Approach: Models, Tasks, Methods and Tools*. 2014.
26. *Matlab with statistics and optimization toolboxes*. The Mathworks Inc.; 2015.
27. Max Kuhn. Contributions from Jed Wing, Steve Weston, Andre Williams, Chris Keefer, Allan Engelhardt, Tony Cooper, Zachary Mayer, Brenton Kenkel, the R Core Team, Michael Benesty, Reynald Lescarbeau, Andrew Ziem, Luca Scrucca, Yuan Tang, Can Candan and Tyler Hunt. (2018). caret: Classification and Regression Training. R package version 6.0-80. <https://CRAN.R-project.org/package=caret>.
28. R Core Team (2018). R: A language and environment for statistical computing. R Foundation for Statistical Computing, Vienna, Austria. URL <https://www.R-project.org/>.
29. Savic RM, Karlsson MO. Importance of Shrinkage in Empirical Bayes Estimates for Diagnostics: Problems and Solutions. *AAPS J*. 2009;11:558–69.
30. Pollard JW. Defining Metastatic Cell Latency. *N Engl J Med*. 2016;375:280–2.

31. Kuhn M, Johnson K. Applied predictive modeling. Springer; 2013.
32. Francia G, Cruz-Munoz W, Man S, Xu P, Kerbel RS. Mouse models of advanced spontaneous metastasis for experimental therapeutics. *Nat Rev Cancer*. 2011;11:135–41.
33. Paez-Ribes M, Allen E, Hudock J, Takeda T, Okuyama H, Viñals F, et al. Antiangiogenic therapy elicits malignant progression of tumors to increased local invasion and distant metastasis. 2009;15:220–31.
34. Reiter JG, Makohon-Moore AP, Gerold JM, Heyde A, Attiyeh MA, Kohutek ZA, et al. Minimal functional driver gene heterogeneity among untreated metastases. *Science*. 2018;361:1033–7.
35. Haeno H, Gonen M, Davis MB, Herman JM, Iacobuzio-Donahue CA, Michor F. Computational Modeling of Pancreatic Cancer Reveals Kinetics of Metastasis Suggesting Optimum Treatment Strategies. *Cell*. 2012;148:362–75.
36. Hartung N, Mollard S, Barbolosi D, Benabdallah A, Chapuisat G, Henry G, et al. Mathematical modeling of tumor growth and metastatic spreading: validation in tumor-bearing mice. *Cancer Res*. 2014;74:6397–407.
37. Benzekry S, André N, Benabdallah A, Ciccolini J, Faivre C, Hubert F, et al. Modelling the impact of anticancer agents on metastatic spreading. *Math Model Nat Phenom*. 2012;7:306–36.
38. Benzekry S, Hahnfeldt P. Maximum tolerated dose versus metronomic scheduling in the treatment of metastatic cancers. *J Theor Biol*. 2013;335:235–44.
39. Bridgeman VL, Vermeulen PB, Foo S, Bilecz A, Daley F, Kostaras E, et al. Vessel co-option is common in human lung metastases and mediates resistance to anti-angiogenic therapy in preclinical lung metastasis models. *J Pathol*. 2017;241:362–74.
40. Wu FTH, Xu P, Chow A, Man S, Krüger J, Khan KA, et al. Pre- and post-operative anti-PD-L1 plus anti-angiogenic therapies in mouse breast or renal cancer models of micro- or macro-metastatic disease. *Br J Cancer*. 2019;120:196–206.
41. Krop I, Ismaila N, Andre F, Bast RC, Barlow W, Collyar DE, et al. Use of Biomarkers to Guide Decisions on Adjuvant Systemic Therapy for Women With Early-Stage Invasive Breast Cancer: American Society of Clinical Oncology Clinical Practice Guideline Focused Update. *J Clin Oncol*. 2017;35:2838–47.
42. Cardoso F, van't Veer LJ, Bogaerts J, Slaets L, Viale G, Delaloge S, et al. 70-Gene Signature as an Aid to Treatment Decisions in Early-Stage Breast Cancer. *N Engl J Med*. 2016;375:717–29.
43. Senkus E, Kyriakides S, Ohno S, Penault-Llorca F, Poortmans P, Rutgers E, et al. Primary breast cancer: ESMO Clinical Practice Guidelines for diagnosis, treatment and follow-up. *Ann Oncol*. 2015;26 Suppl 5:v8–30.
44. Ravdin PM, Siminoff LA, Davis GJ, Mercer MB, Hewlett J, Gerson N, et al. Computer program to assist in making decisions about adjuvant therapy for women with early breast cancer. *J Clin Oncol*. 2001;19:980–91.

45. Wishart GC, Azzato EM, Greenberg DC, Rashbass J, Kearins O, Lawrence G, et al. PREDICT: a new UK prognostic model that predicts survival following surgery for invasive breast cancer. *Breast Cancer Res.* 2010;12:R1.
46. Hortobagyi GN, Connolly JL, DOrsi CJ, Edge S, Mittendorf E, Rugo HS, et al. AJCC Cancer Staging Manual - Breast Cancer. In: Amin MB, Edge S, Greene F, Byrd DR, Brookland RK, Washington MK, et al., editors. *AJCC Cancer Staging Man.* Springer International Publishing; 2017.
47. Nicolò C, Périer C, Prague M, Bellera C, MacGrogan G, Saut O, et al. Machine Learning and Mechanistic Modeling for Prediction of Metastatic Relapse in Early-Stage Breast Cancer. *JCO Clin Cancer Inform.* 2020;4:259–74.
48. Topol EJ. High-performance medicine: the convergence of human and artificial intelligence. *Nat Med.* 2019;25:44–56.
49. Perou CM, Sørlie T, Eisen MB, van de Rijn M, Jeffrey SS, Rees CA, et al. Molecular portraits of human breast tumours. *Nature.* 2000;406:747–52.
50. Limkin EJ, Sun R, Dercle L, Zacharaki EI, Robert C, Reuzé S, et al. Promises and challenges for the implementation of computational medical imaging (radiomics) in oncology. *Ann Oncol.* 2017;28:1191–206.
51. Kather JN, Krisam J, Charoentong P, Luedde T, Herpel E, Weis C-A, et al. Predicting survival from colorectal cancer histology slides using deep learning: A retrospective multicenter study. *Butte AJ, editor. PLOS Med.* 2019;16:e1002730.
52. Kourou K, Exarchos TP, Exarchos KP, Karamouzis MV, Fotiadis DI. Machine learning applications in cancer prognosis and prediction. *Comput Struct Biotechnol J.* 2015;13:8–17.
53. Yerushalmi R, Woods R, Ravdin PM, Hayes MM, Gelmon KA. Ki67 in breast cancer: prognostic and predictive potential. *Lancet Oncol.* 2010;11:174–83.
54. Dowsett M, Nielsen TO, A'Hern R, Bartlett J, Coombes RC, Cuzick J, et al. Assessment of Ki67 in breast cancer: recommendations from the International Ki67 in Breast Cancer working group. *J Natl Cancer Inst.* 2011;103:1656–64.
55. Imbs D-C, El Cheikh R, Boyer A, Ciccolini J, Mascaux C, Lacarelle B, et al. Revisiting Bevacizumab + Cytotoxics Scheduling Using Mathematical Modeling: Proof of Concept Study in Experimental Non-Small Cell Lung Carcinoma. *CPT Pharmacomet Syst Pharmacol.* 2018;7:42–50.
56. Rothschild S, Zippelius A, Savic S, Gonzalez M, Weder W, Xyrafas A, et al. SAKK 16/14: Anti-PD-L1 antibody durvalumab (MEDI4736) in addition to neoadjuvant chemotherapy in patients with stage IIIA(N2) non-small cell lung cancer (NSCLC)—A multicenter single-arm phase II trial. *J Clin Oncol.* 2018;36:TPS8584–TPS8584.
57. Ciccolini J, Barbolosi D, André N, Benzekry S, Barlesi F. Combinatorial immunotherapy strategies: most gods throw dice, but fate plays chess. *Ann Oncol. Elsevier;* 2019;30:1690–1.
58. Reguera-Nuñez E, Man S, Xu P, Kerbel RS. Preclinical impact of high dose intermittent antiangiogenic tyrosine kinase inhibitor pazopanib in intrinsically resistant tumor models. *Angiogenesis.* 2018;21:793–804.

59. Ratain MJ, Goldstein DA. Time Is Money: Optimizing the Scheduling of Nivolumab. *J Clin Oncol*. 2018;JCO.18.00045-4.
60. Ciccolini J, Benzekry S, Barlesi F. Deciphering the response and resistance to immune-checkpoint inhibitors in lung cancer with artificial intelligence-based analysis: when PIONeeR meets QUANTIC. *Br J Cancer*. Nature Publishing Group; 2020;1–2.

Figure 1

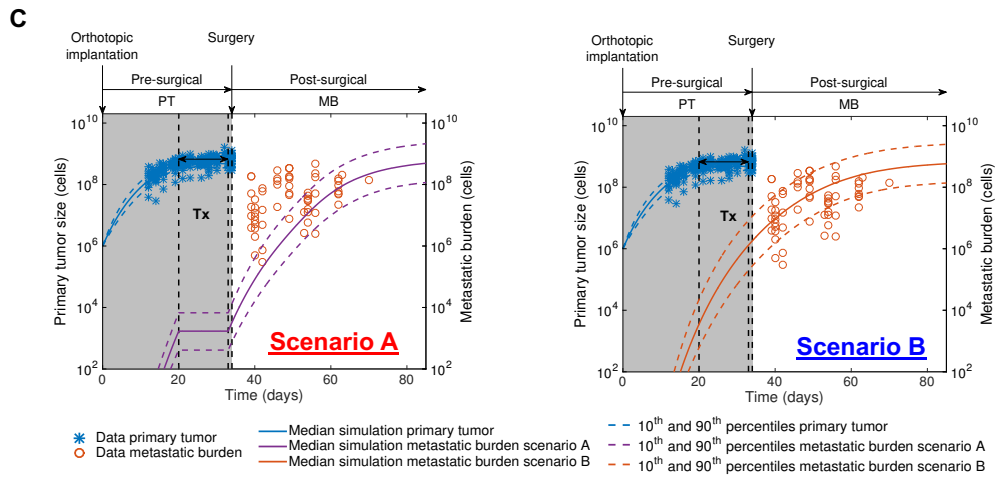
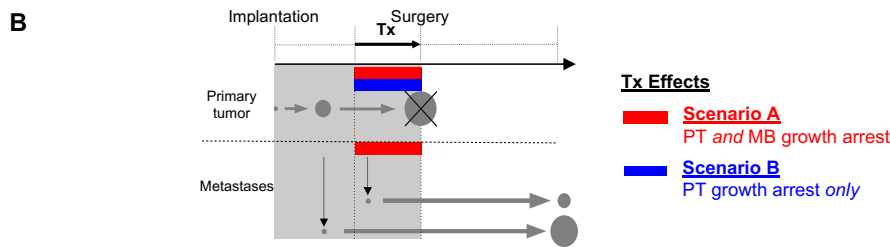
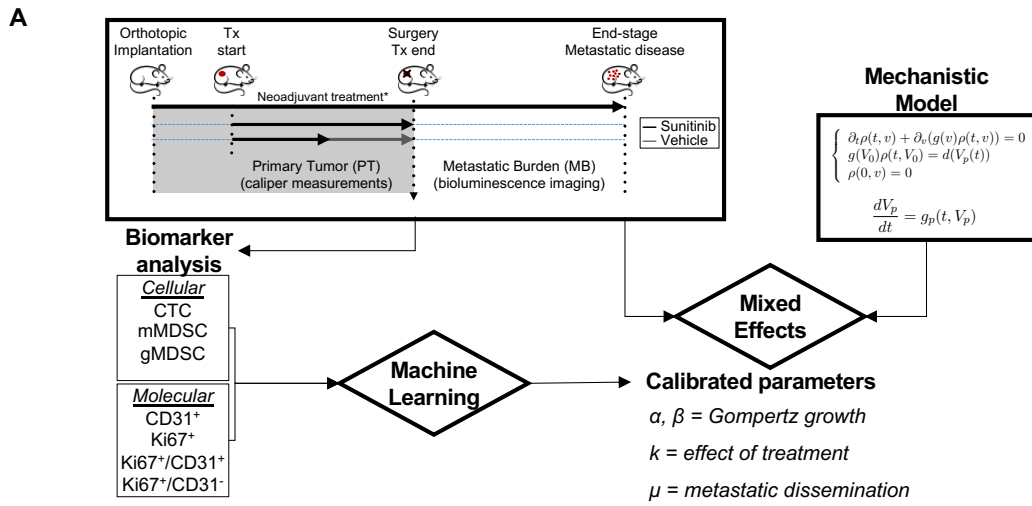


Figure 1: Mathematical modeling reveals differential effects of neoadjuvant sunitinib treatment on primary tumor and metastatic growth.

(A) Schematic of the study. Data from an ortho-surgical, human xenograft animal model of neoadjuvant sunitinib breast cancer treatment were fitted using a mixed-effects statistical framework. This provided calibrated parameters for each animal. Machine learning algorithms were used to assess the predictive power of molecular and cellular biomarkers to predict the metastatic dissemination parameter μ and quantify metastatic aggressiveness. Biological and numerical parameters quantified at end of therapy and at time of surgery were implemented into a survival model.

(B) Schematic of tested hypotheses of the effect of neoadjuvant sunitinib Tx on primary tumor and metastatic growth and dissemination through mechanistic mathematical modeling. Scenario A = growth arrest on both primary and secondary tumors. Scenario B = growth arrest on primary tumor only.

(C) Predicted simulations of Scenarios A and B using parameters calibrated from a previous study [Benzekry et al., Cancer Res, 2016] involving untreated (vehicle) animals only. Data plotted here (LM2-4^{LUC+} bioluminescent human breast cancer cells orthotopically injected in mice) was not used to estimate the model parameters.

*Tx, treatment; PT, primary tumor; MB, metastatic burden. *See methods for additional details on animal experiments, treatment dose and duration, and mechanistic model.*

Figure 2

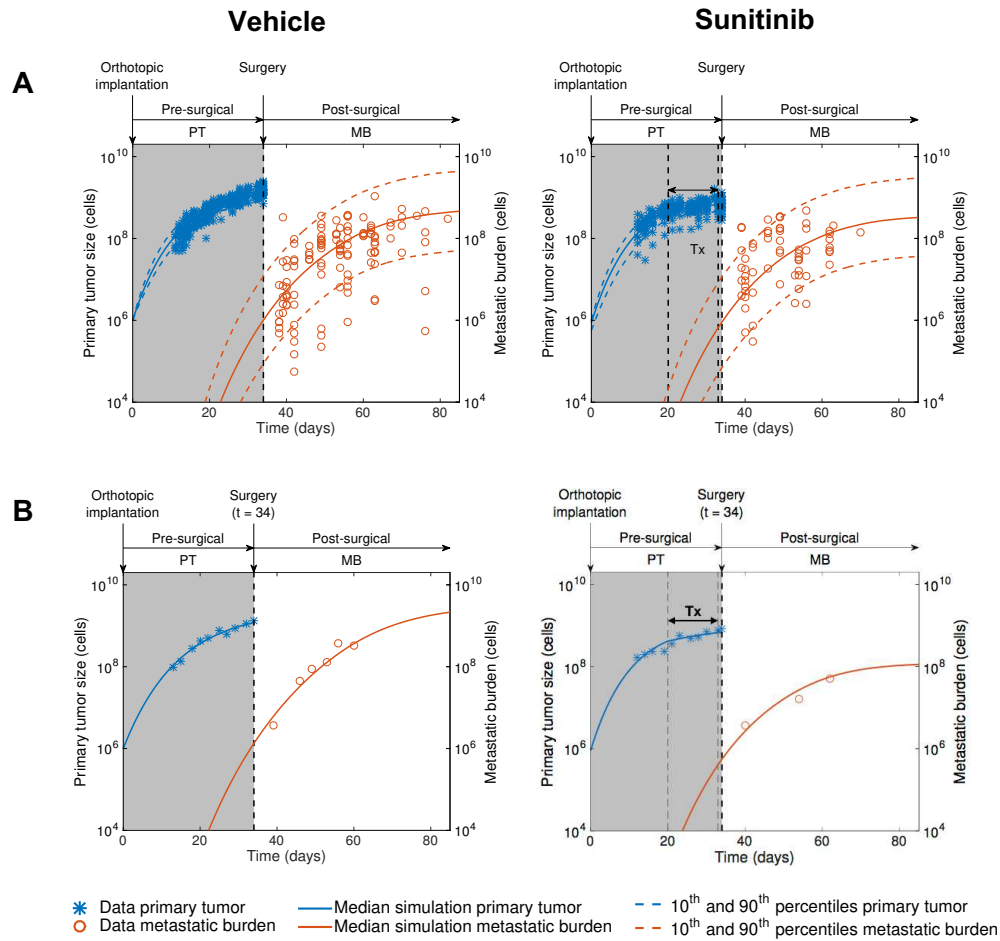


Figure 2: Calibration and validation of a kinetics-pharmacodynamics (K-PD) mathematical model for neoadjuvant sunitinib treatment effect on pre- and post-surgical tumor growth

Pre- and postsurgical growth of LM2-4^{LUC+} human metastatic breast carcinomas were measured in multiple groups involving different neoadjuvant treatment modalities (doses and durations). The mathematical model was fitted to the experimental data using a mixed-effects population approach (n=104 animals in total).

(A) Comparison of the simulated model population distribution (visual predictive check) for vehicle and neoadjuvant sunitinib treatment (60mg/kg/day) 14 days prior to surgery.

(B) Examples of individual dynamics.

Tx, treatment; PT, primary tumor; MB, metastatic burden.

Figure 3

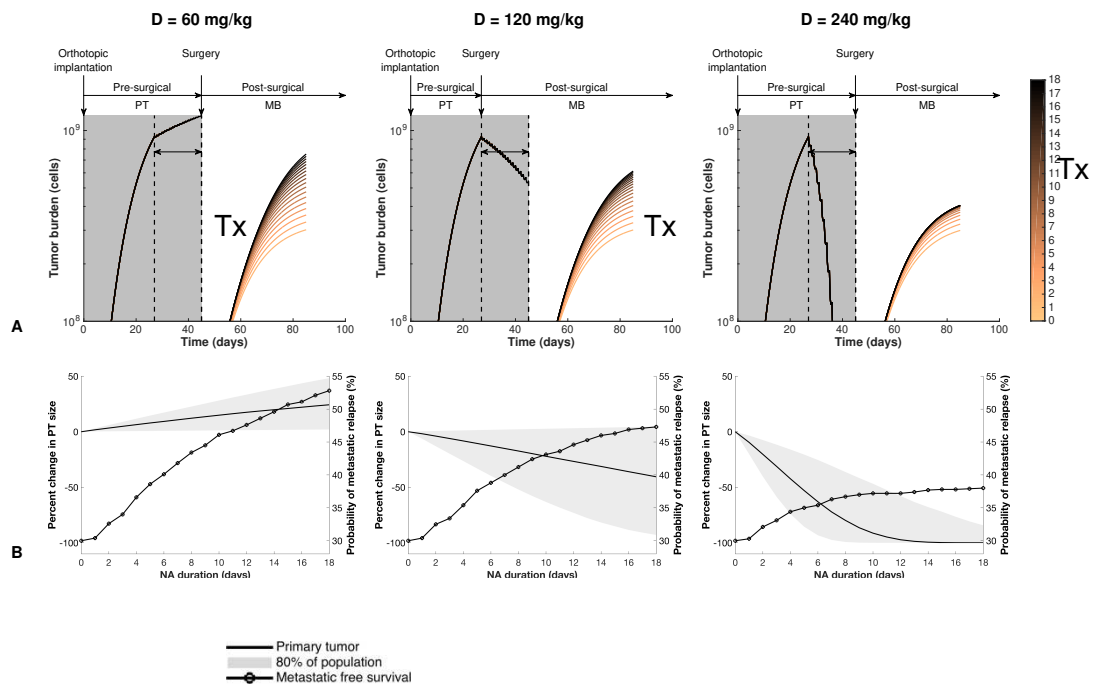


Figure 3: Simulations of varying neoadjuvant treatment duration quantify contrasted impact on primary tumor size reduction and risk of metastatic relapse

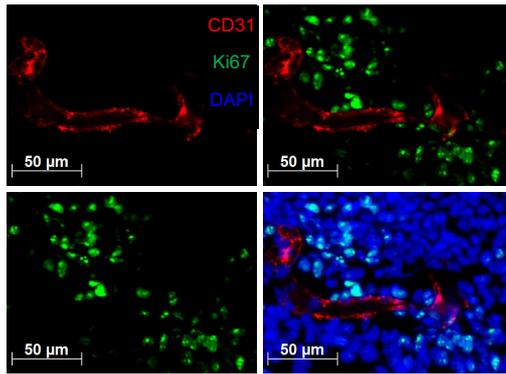
Using model parameters calibrated from data of our ortho-surgical animal model of breast cancer neoadjuvant treatment (NAT), simulations were conducted for a duration of NAT varying between 0 (light color) and 18 (dark color) days, for three dose levels (60 mg/kg, 120 mg/kg and 240 mg/kg).

(A) Predicted simulations of pre-surgical primary tumor and post-surgical metastatic kinetics. Primary tumor growth curves are not distinguishable because they are all superimposed until time of surgery.

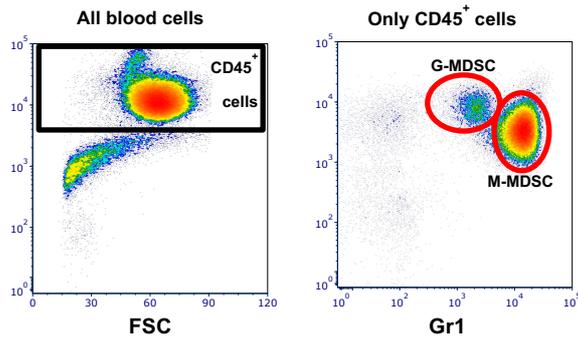
(B) Population-level predictions of final primary tumor size (solid line and grey area) and probability of metastatic relapse as functions of duration of neoadjuvant treatment, which delays surgical removal of primary tumor (circled line). Inter-individual variability simulated from population distribution of the parameters learned from the data ($n = 1000$ virtual subjects).

Figure 4

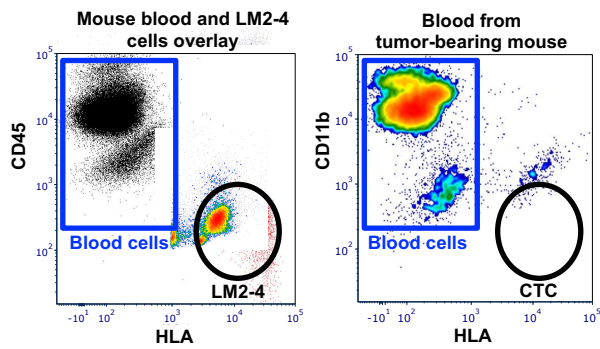
A



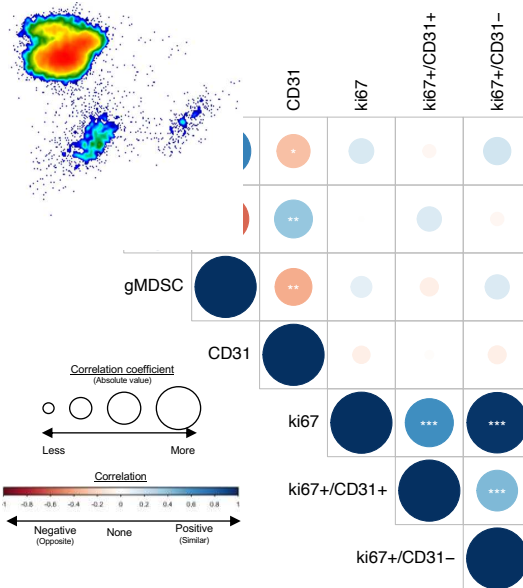
B



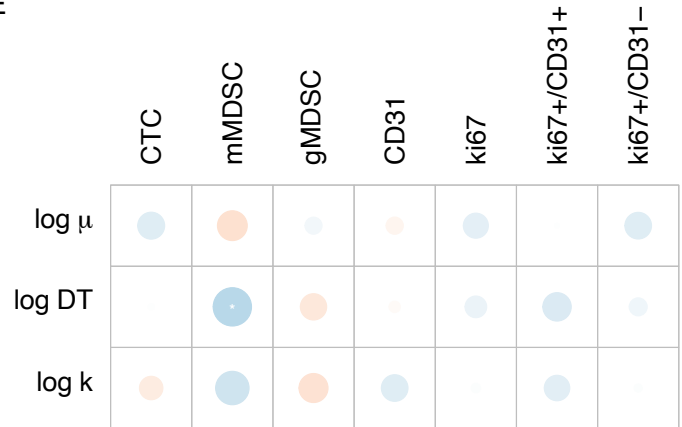
C



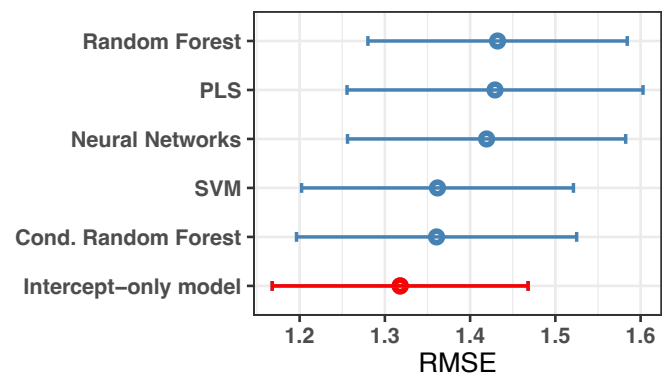
D



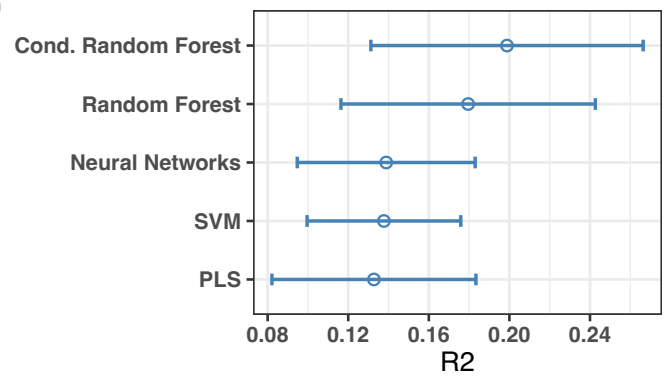
E



F



G



H

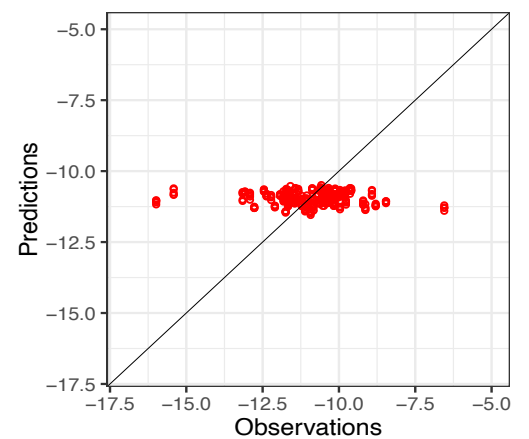


Figure 4: Use of machine learning algorithms based on presurgical molecular and cellular markers to predict metastatic dissemination parameter ‘ μ ’.

(A-C) Examples of molecular and cellular biomarker analysis.

(A) Proliferating endothelial cell identification by immunofluorescence. Tissue sections from resected tumors were stained with antibodies against mouse CD31 (red) and mouse Ki67 (green) and counterstained with DAPI (blue). Single channel and merged images are shown. Yellow arrows show proliferating endothelial cells which were counted manually.

(B) Myeloid-Derived Suppressor Cells (MDSC) quantification by flow cytometry. Whole blood was stained with anti-mouse antibodies for CD45, CD11b, and Gr1. After selection of CD45 positive cells MDSCs were analyzed based on CD11b and Gr1 levels. Monocytic-MDSC (M-MDSC) are CD11b+/Gr1high and granulocytic-MDSC (G-MDSC) are CD11b+/Gr1Medium. Examples of MDSC in untreated and treated animals are shown.

(C) CTC quantification by flow cytometry. CTCs for xenografts were identified using anti-human HLA. Blood was stained with anti-mouse CD45 and anti-human HLA. Blood and LM2-4 cell samples were overlaid in a dot plot to identify and create the gates for CTCs. Once the gates were created CTC were identified in blood of tumor-bearing mice.

(D) Pearson correlation coefficients between biomarkers. Blue (resp. red) color indicates positive (resp. negative) correlation, with size of the circle proportional to the R^2 correlation coefficient. * $p < 0.05$, ** $p < 0.01$, *** $p < 0.001$.

(E) Univariate correlations between the biomarkers and the mathematical parameters. DT = doubling time.

(F) Cross-validated Root Mean Square Error (RMSE) across different machine learning regression models (see methods) utilizing the values of the biomarkers for predicting $\log(\mu)$. To assess the significance of the covariate in the models, RMSE were compared against the value of this metric obtained using a only-intercept model. Bars are 95% confidence intervals. Shown in red is the model with lowest RMSE. PLS = Partial Least Squares. SVM = Support Vector Machines

(G) Cross validated R^2 with 95% confidence intervals.

(H) Predictions versus observations for the conditional random forest algorithm.

	Parameter (Unit)	Meaning	Median	CV (%)	r.s.e. (%)
Metastatic model	μ (cell ⁻¹ · day ⁻¹)	dissemination coefficient	$2.12 \cdot 10^{-11}$	$1.48 \cdot 10^3$	17.3
	α (day ⁻¹)	gompertzian growth parameter	1.94	18.1	2
	β (day ⁻¹)	gompertzian growth parameter	0.0911	19.7	2.21
	λ (day ⁻¹)	in vitro proliferation rate	0.837 (fixed)	-	-
	k (L/mg)	drug efficacy	0.446	32.1	6.34
	k_e (day ⁻¹)	drug elimination rate	3.26 (fixed)	-	-
	V_d (L/kg)	volume of distribution	12 (fixed)	-	-
Survival model	T_e (day)	scale parameter	32.3	11.5	11.4
	β_μ (unitless)	covariate coefficient	-0.066	-	15.8
	s (unitless)	shape parameter	17.9	-	21.6

Table 1: Parameter estimates of the metastatic and survival models obtained by likelihood maximization via the SAEM algorithm. In the survival model, $\log(\mu)$ has been included as covariate on the scale parameter T_e : $\log(T_e) = \log(T_e, pop) + \beta \log(\mu) + \eta$.

Abbreviations: CV, coefficient of variation computed as the ratio of the standard deviation and the median of the estimated parameter distribution; r.s.e., residual standard error.

Supplementary Table:

Table S1: Neoadjuvant treatment schedules and doeses

Table S1:

Group	N	Duration (Days)			Surgery (DPI)	Modeling	Abbrev.
		Sunitinib (mg/kg/day)					
		120	60	0			
1	6	0	0	14	38	Training	Veh.
2	21	0	0	14	34	Training	Vech.
3	21	0	14	0	34	Training	Su60(14D)
4	6	0	7	7	34	Training	Su60(7D)
5	15	0	3	11	34	Training	Su60(3D)
6	15	3	11	0	34	Training	Su120(3D)/Su60(11D)
7	20	3	0	11	34	Training	Su120(3D)
8	6	3	11	0	38	Validation	Su120(3D)/Su60(11D)
9	6	3	8	3	38	Validation	Su120(3D)/Su60(8D)
10	6	3	4	7	38	Validation	Su120(3D)/Su60(4D)
11	6	3	0	11	38	Validation	Su120(3D)

Table S1: Animal groups showing treatment schedules and dosing during a presurgical neoadjuvant period of 14 days.

Supplementary Figures

Figure S1. Comparison of simulation of therapy (A) vs no therapy (B) on metastases

Figure S2. Population fits of all the groups used to calibrate the model parameters (surgery at day 34)

Figure S3. Representative individual fits of the model for Sunitinib-treated animals

Figure S4. Model predictions in independent datasets (surgery at day 38)

Figure S5. Model diagnostic plots

Figure S6. Distribution of the individual parameters

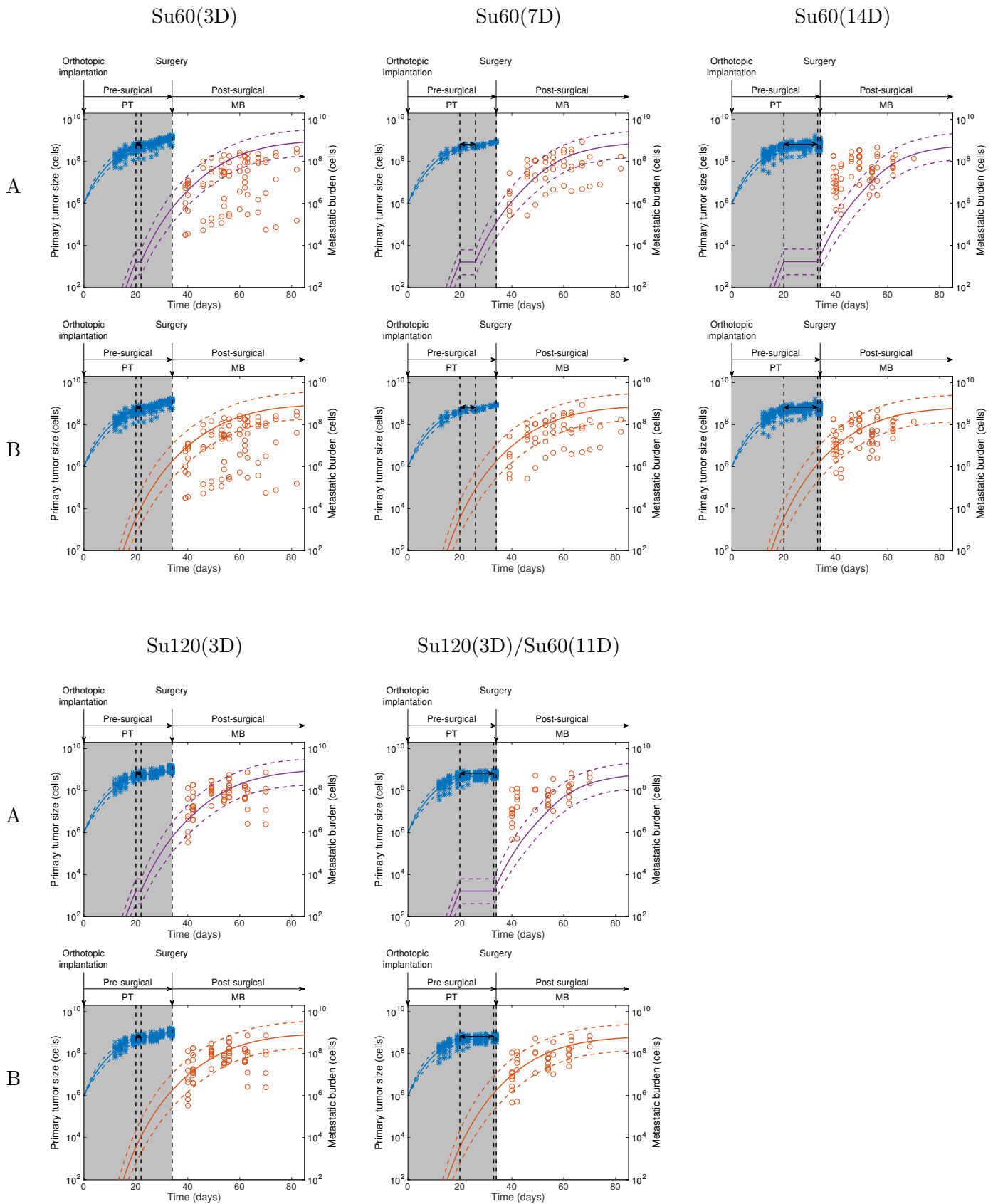
Figure S7. Correlations between random effects

Figure S8. Individual parameters vs covariates

Figure S9. Observed vs Predicted values for the machine learning algorithms

Figure S1. Comparison of simulation of therapy (A) vs no therapy (B) on metastases

Surgery at day 34

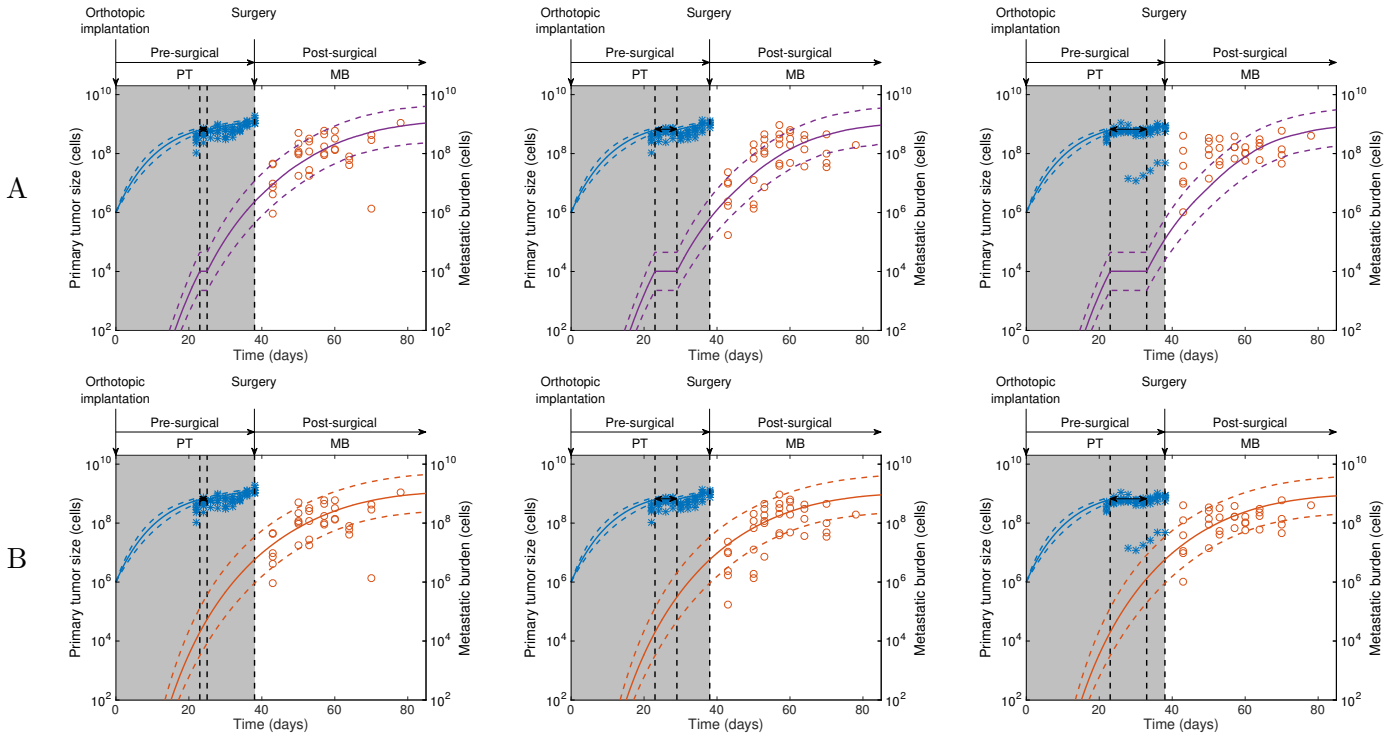


Surgery at day 38

Su120(3D)

Su120(3D)/Su60(4D)

Su120(3D)/Su60(8D)



Su120(3D)/Su60(11D)

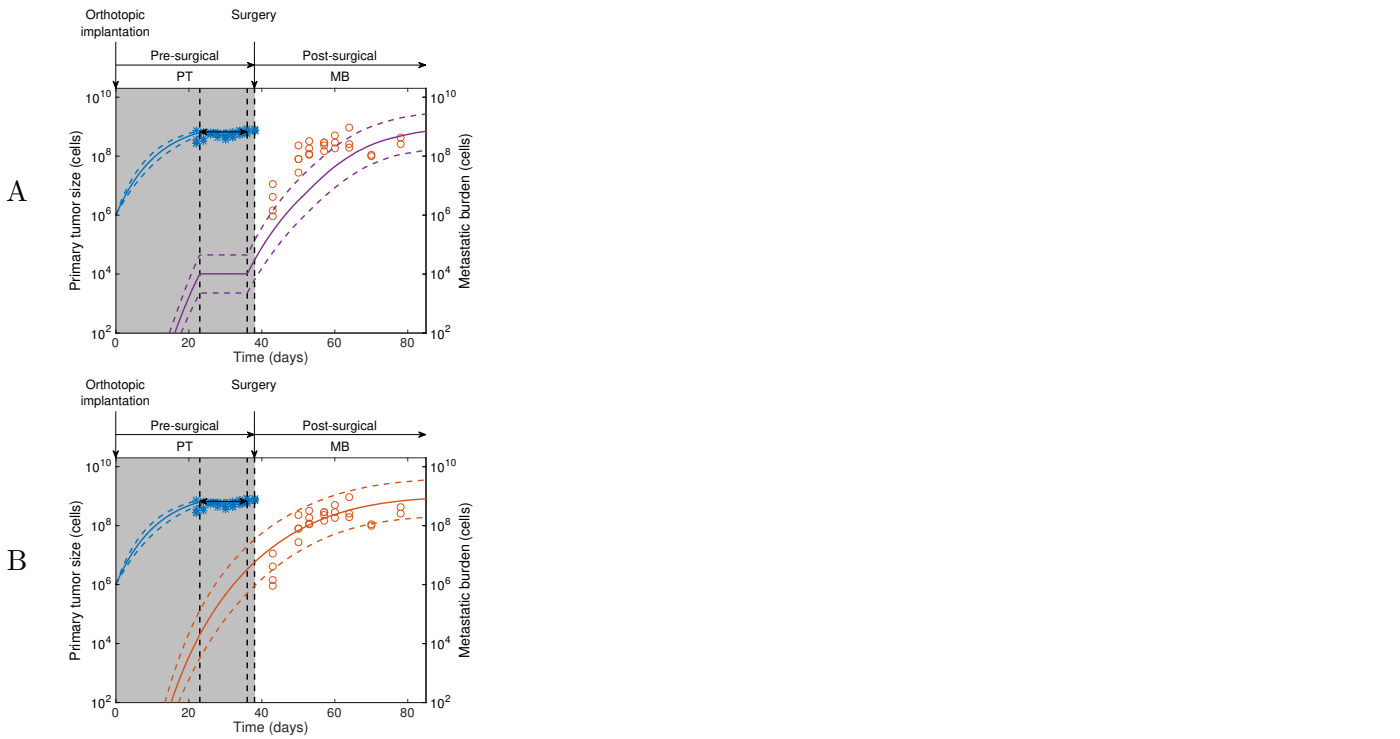


Figure S2. Population fits of all the groups used to calibrate the model parameters (surgery at day 34)

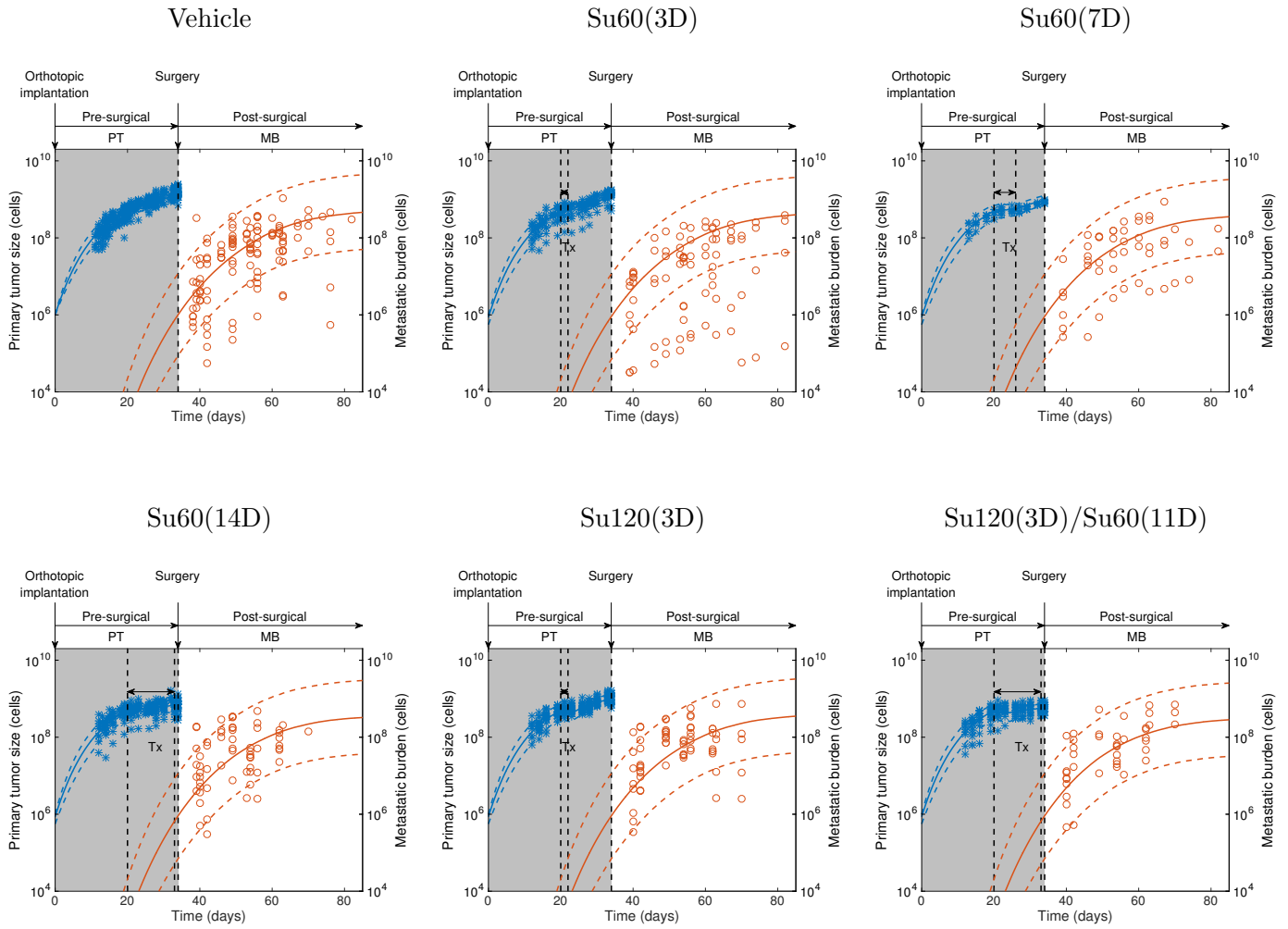


Figure S3. Representative individual fits of the model for Sunitinib-treated animals

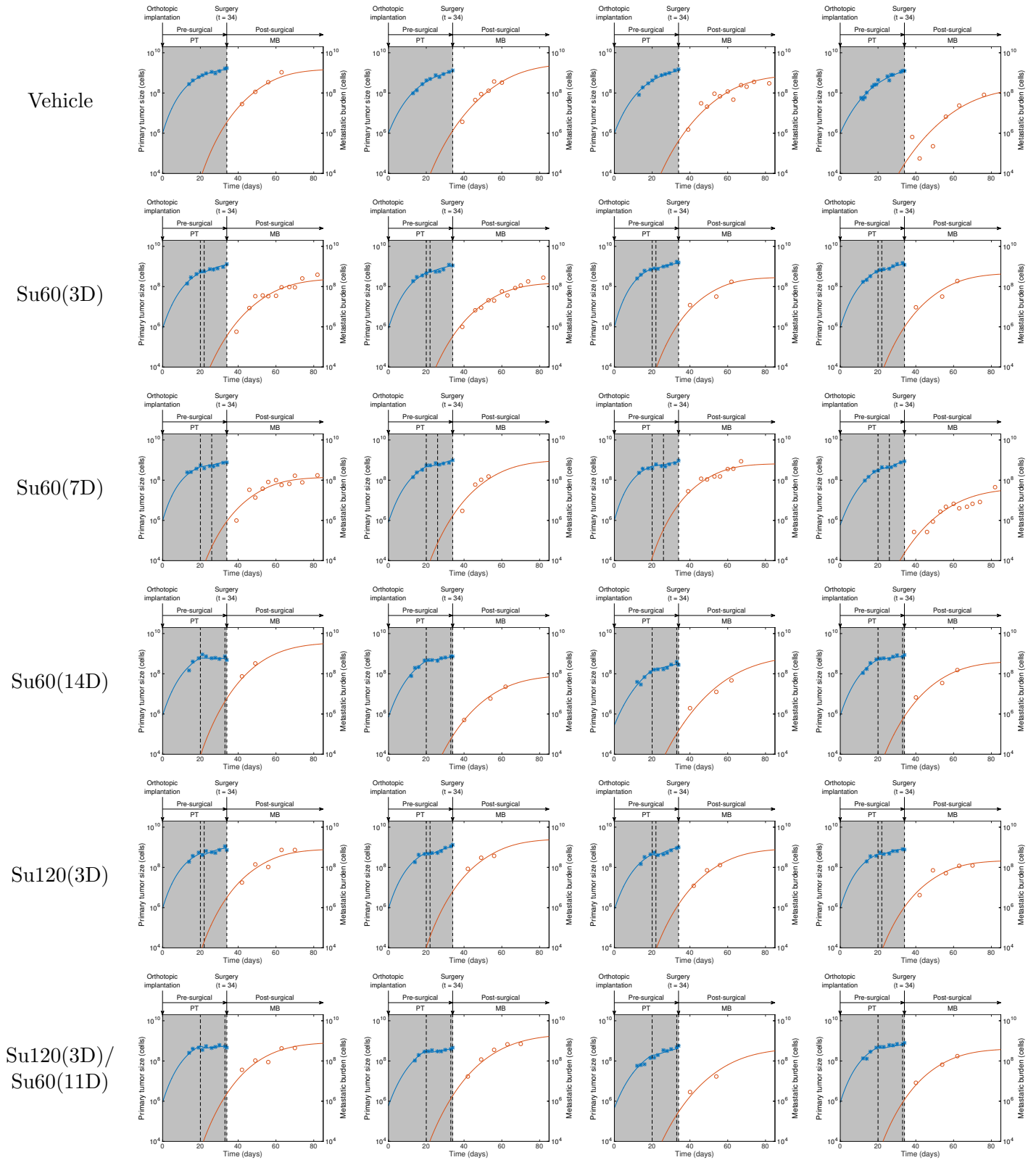


Figure S4. Model predictions in independent datasets (surgery at day 38)

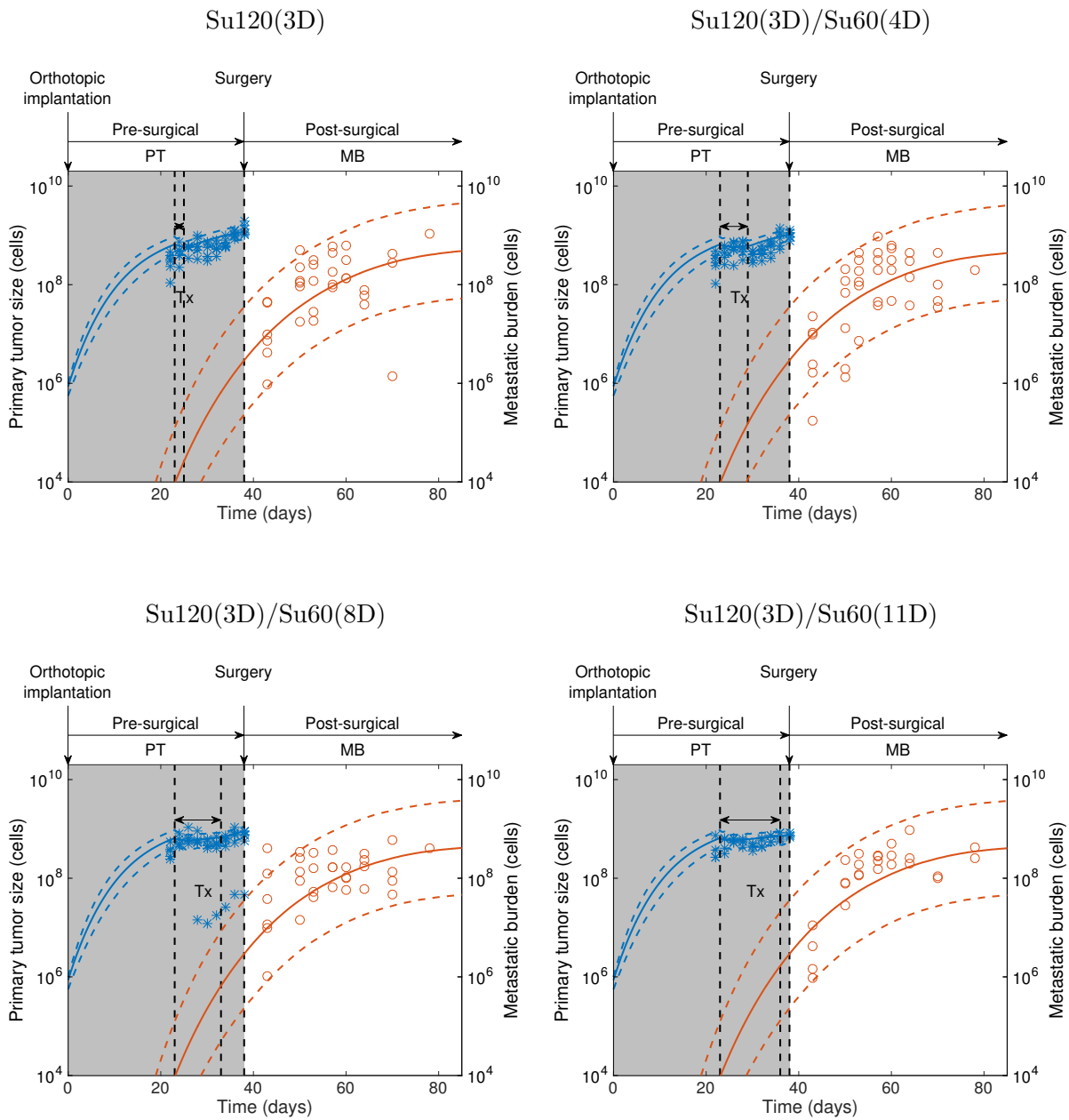
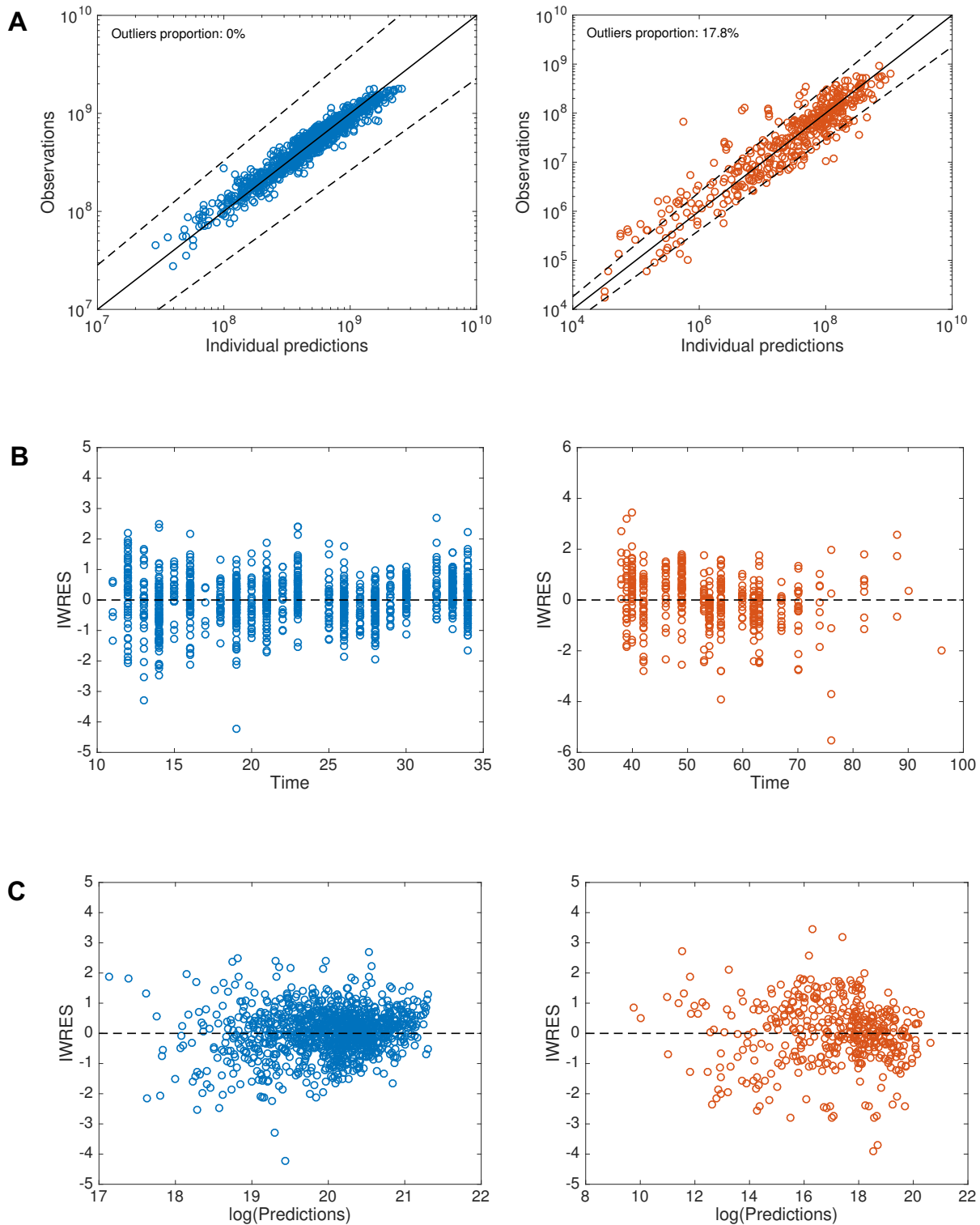


Figure S5. Model diagnostic plots



A) Observation vs. individual prediction. Solid lines are identity lines. Dashed lines represent 90% prediction intervals.
B) Individual weighted residuals (IWRES) vs. time.
C) Individual weighted residuals vs. log-transformed individual predictions.

Figure S6. Distribution of the individual parameters

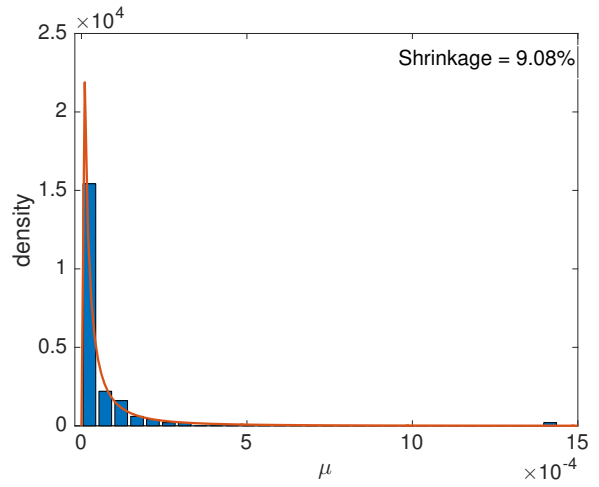
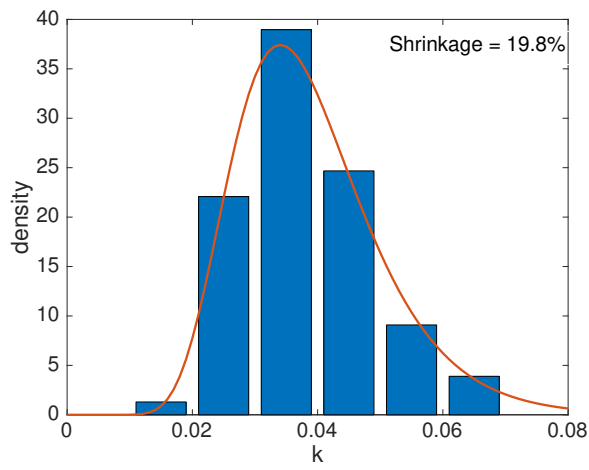
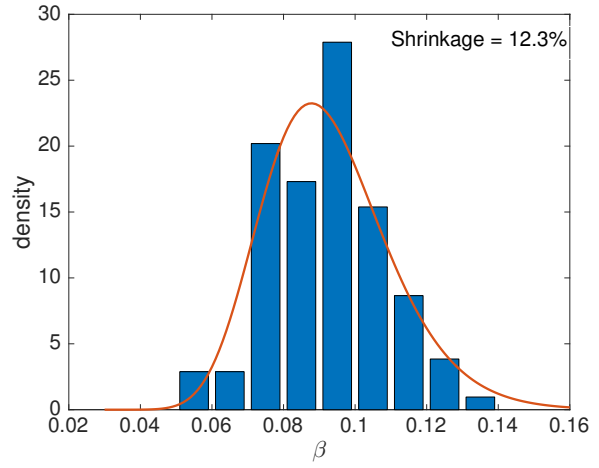
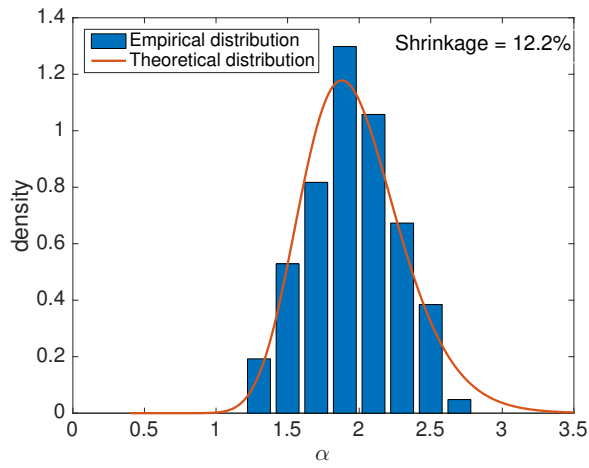


Figure S7. Correlations between random effects

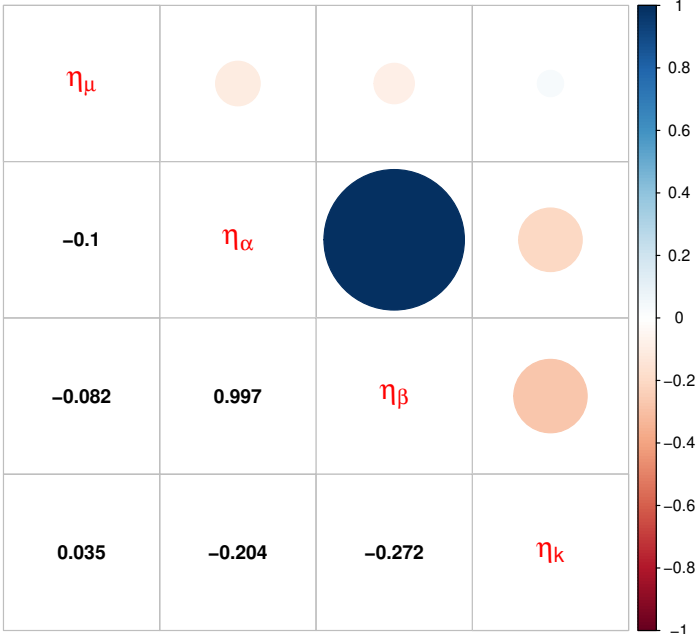


Figure S8. Individual parameters vs covariates

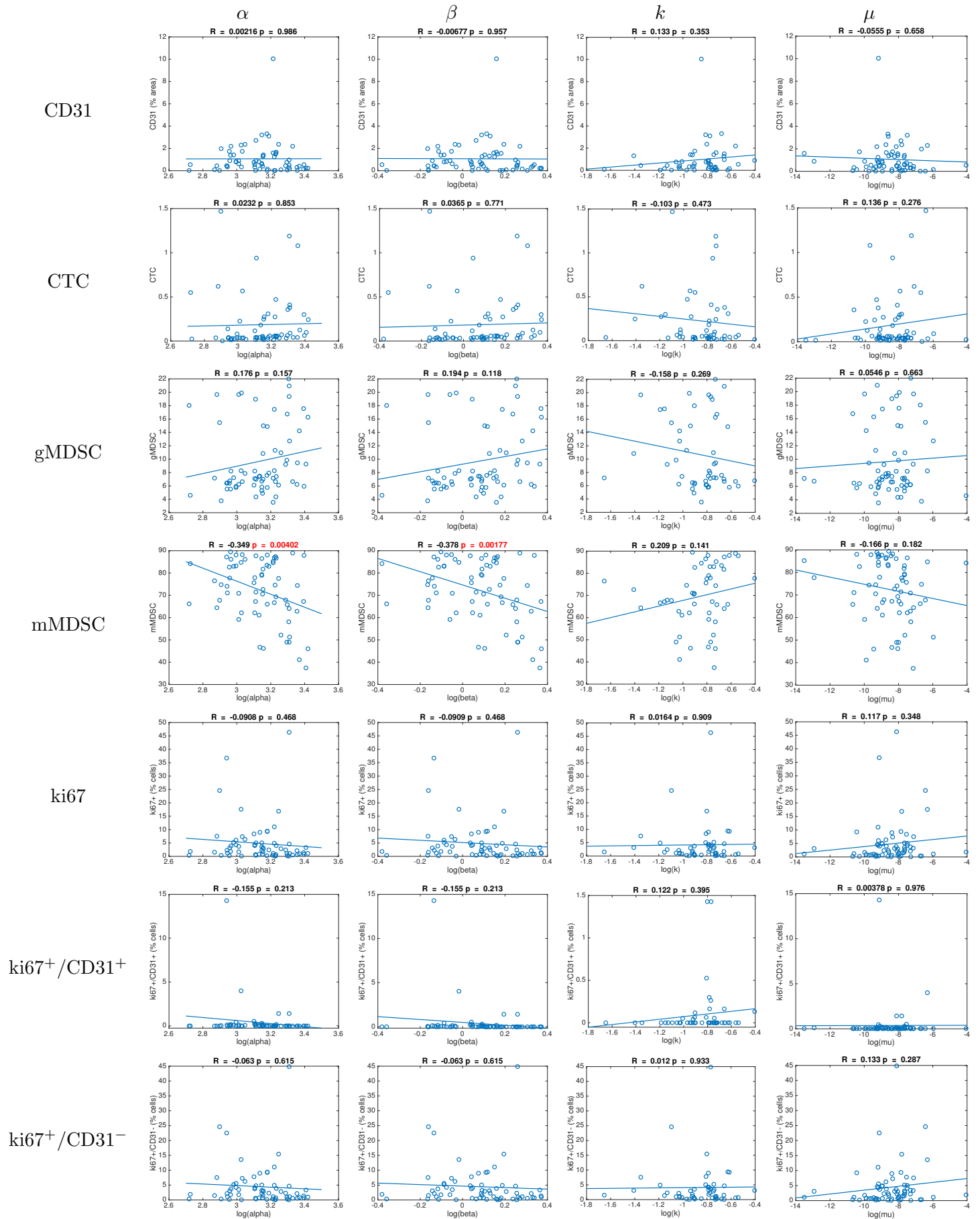
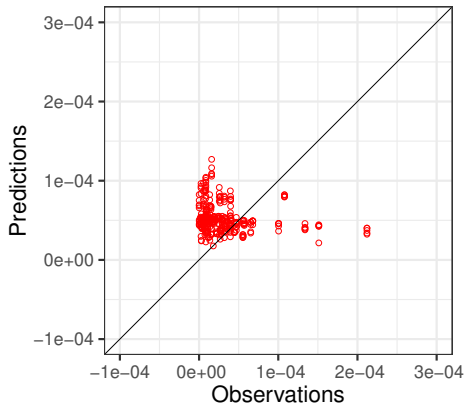


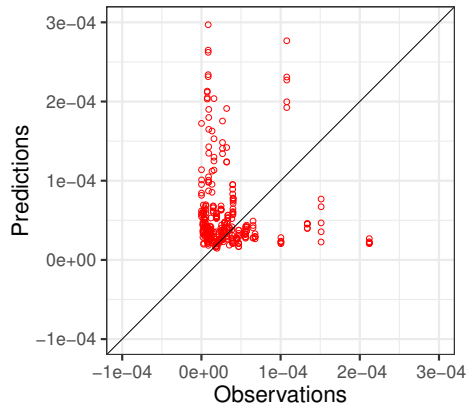
Figure S9. Observed vs Predicted values for the machine learning algorithms

Models for predicting μ

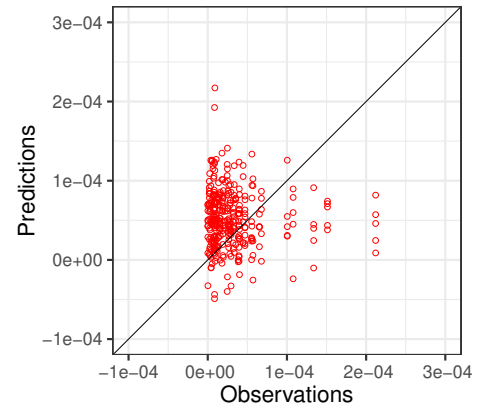
Conditional random forest



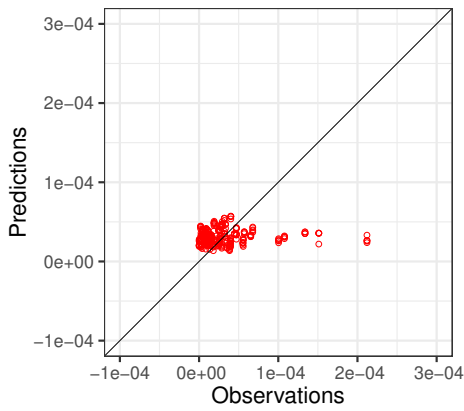
Random forest



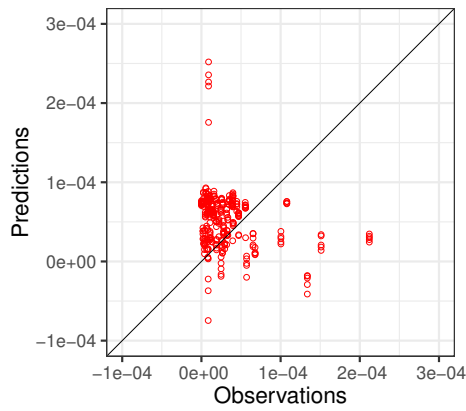
Neural networks



SVM

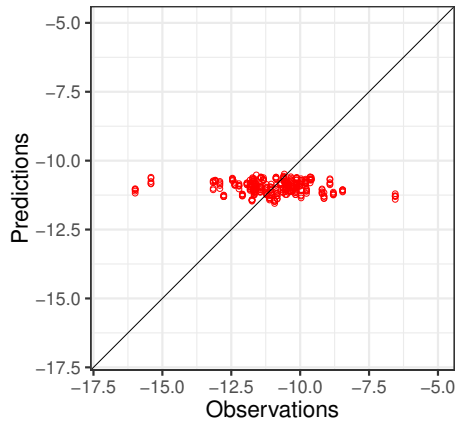


PLS

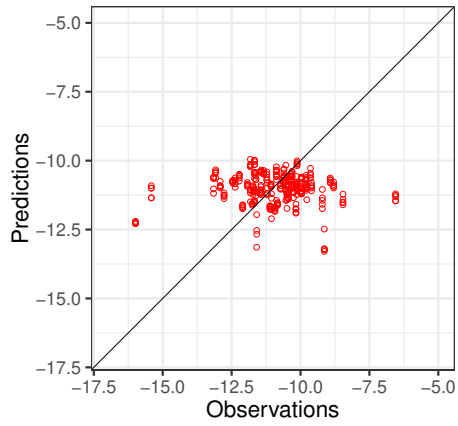


Models for predicting $\log(\mu)$

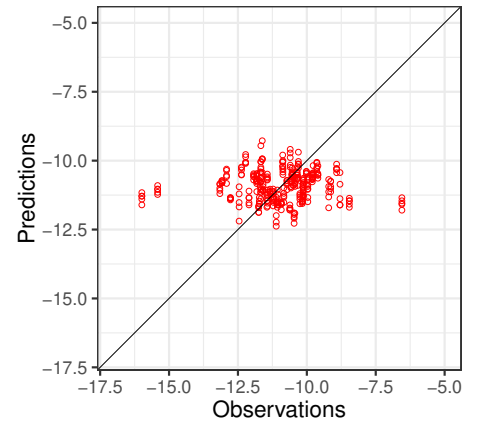
Conditional random forest



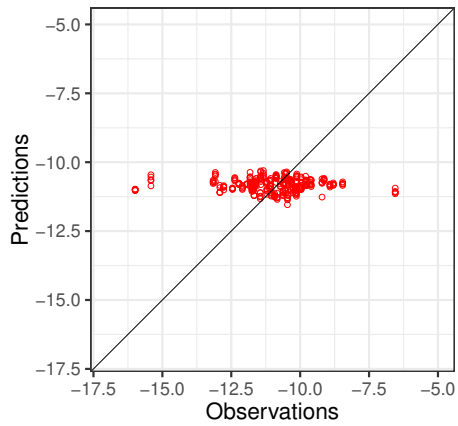
Random forest



Neural networks



SVM



PLS

